https://doi.org/10.5194/egusphere-2026-4732
Preprint. Discussion started: 2 November 2026
© Author(s) 2026. CC BY 4.0 License.

Climatic cycles and potential bias in the relationship between channel steepness and cosmogenic erosion rates

Xianjun Fang[1], Sean D. Willett[1]

[1]Department of Earth and Planetary Sciences, ETH Zurich, Sonneggstrasse 5, 8092 Zurich, Switzerland

Correspondence to: Xianjun Fang (xianjun.fang@eaps.ethz.ch)

Abstract. We investigate the relationship between river channel steepness, catchment-averaged erosion rates from cosmogenic nuclides, and their potential sensitivity to cyclic precipitation rate. Using a one-dimensional longitudinal river-profile model based on the stream power law, we simulate the temporal evolution of channel steepness and erosion rates under a range of cyclic precipitation regimes. Our analysis explores the roles of sinusoidal precipitation characterized by an amplitude (P_a), mean (P_m), period, and uplift rate. We find that the ratio of precipitation amplitude to mean (P_a / P_m) is the primary control on variations in instantaneous catchment-integrated erosion rates (E_{in}), erosion rate averaged over cosmogenic nuclide accumulation time (E_{cos}), and precipitation-modified channel steepness ($k_{s\text{-}Q}$). These oscillations lead to deviations of E_{cos} and $k_{s\text{-}Q}$ from uplift rates and the corresponding channel steepness, and in regions with high P_a / P_m values, the regression between erosion rate and channel steepness becomes unreliable, with extreme phase differences potentially reversing their expected relationship. To address these limitations, we introduce a new erosion rate metric, Cosmogenic-constrained cycle-mean erosion rate ($E_{cos\text{-}Qm}$), which represents the mean erosion rate over a climatic cycle, derived from cosmogenic nuclide concentrations combined with information on climate cyclicity. Using 1D river profile modelling, combined with $k_{s\text{-}Qeff}$, which is the channel steepness modified by effective precipitation over climatic cycles, we demonstrate that the relationship between $E_{cos\text{-}Qm}$ and $k_{s\text{-}Qeff}$ remains stable across sinusoidal, insolation-based and proxy-based precipitation cycles, making them more reliable indicators of long-term erosion or uplift rates. We apply this approach to granite catchments in the Three Rivers region as a natural case study to evaluate the performance of paleo-precipitation-integrated erosion rate and channel steepness metrics, $E_{cos\text{-}Qm}$ and $k_{s\text{-}Qeff}$. The results demonstrate that catchments with higher P_a / P_m values exhibit larger discrepancies between E_{cos} from $E_{cos\text{-}Qm}$, and $k_{sn\text{-}Q}$ from $k_{sn\text{-}Qeff}$, highlighting the importance of accounting for temporal precipitation variability in interpreting erosion-steepness relationships.

1 Introduction

Fluvial incision is a key surface process in shaping landscapes influenced by factors such as channel slope and channel width (Howard and Kerby, 1983; Howard, 1994; Tucker and Slingerland, 1994). The stream power law suggests that channel steepness (k_s), a geomorphic metric that represents slope normalized by discharge, is proportional to erosion rates (Howard

https://doi.org/10.5194/egusphere-2026-4732
Preprint. Discussion started: 2 November 2026
© Author(s) 2026. CC BY 4.0 License.

and Kerby, 1983; Howard, 1994; Whipple and Tucker, 1999). Since discharge data are often unavailable, models, including the stream power model, typically assume discharge is proportional to drainage area. This assumption simplifies the calculation of channel steepness, enabling widespread application using high-resolution digital elevation model (DEM) data.

In regions with spatial variations in precipitation, it has been suggested that precipitation data, rather than drainage area alone, should be incorporated into models, given that it is the discharge in the river that governs incision physics (Roe et al., 2002; Finlayson and Montgomery, 2003). To account for spatial precipitation variation, modern precipitation-modified channel steepness ($k_{s\text{-}Q}$) has been introduced (Ferrier et al., 2013; Yang et al., 2015; Adams et al., 2020; Leonard and Whipple, 2021). This metric is normalized by both drainage area and modern precipitation, under the assumption that all precipitation is converted to runoff. This approach provides a treatment of the spatial variability of precipitation rate, but assumes a temporally stable climate. In many regions, precipitation varies through time, for example, associated with glacial-interglacial climatic cycles. High-frequency climatic oscillations have been shown to have limited impact on river profile form in detachment-limited systems (Goren, 2016), but channel steepness metrics are typically calculated using a single value for precipitation rate, so if this has varied significantly over recent history, the channel steepness metric could be biased with respect to the average precipitation over a cycle. To address this, Wolpert and Schoenbohm (2025) introduced a different metric, $k_{s\text{-}Qeff}$, which incorporates an effective discharge that produces the same cumulative erosion as time-varying discharge over a climate cycle.

Geomorphic metrics are commonly evaluated against catchment-averaged erosion rates derived from cosmogenic nuclides to test geomorphic process laws and parameters. This analysis has been compared to k_s (Ouimet et al., 2009; DiBiase et al., 2010) in order to test whether channel steepness predicts erosion rate. Spatial variations in precipitation strongly influence erosional efficiency, with wetter climates generally producing lower fluvial relief for a given erosion rate (Ferrier et al., 2013; Marder and Gallen, 2023). Correspondingly, $k_{s\text{-}Q}$ performs well in such settings, showing proportional relationships with cosmogenic erosion rates within similar lithologies (Whipple et al., 2023; Leonard et al., 2024). However, cosmogenic isotopes accumulate over timescales that overlap with Milankovitch-scale climate cycles, suggesting some dependence on temporal precipitation changes. Furthermore, depending on erosion rates and the period of climatic cycles, cosmogenic isotopes may integrate erosion over only partial cycles. As a result, cosmogenic erosion rates may deviate from the long-term mean and differ from instantaneous erosion rates. Compared with instantaneous erosion rates, cosmogenic erosion rates generally exhibit reduced variability and a delayed response to climatic fluctuations (Mudd, 2017; Skov et al., 2019).

Although channel steepness metrics and cosmogenic erosion rates are widely used to infer surface processes, the influence of Milankovitch-scale precipitation cycles on their relationship deserves further investigation. In this study, we develop a one-dimensional longitudinal river profile model incorporating cyclic precipitation fluctuations in order to explore how catchment-averaged erosion rates and channel steepness vary spatially and temporally under cyclic climate change. Our primary objective is to examine how precipitation variations during climatic cycles introduce systematic bias in the relationship between $k_{s\text{-}Q}$ and cosmogenic nuclide-derived erosion rates (E_{cos}). Based on our model, we introduce a new metric, cosmogenic-informed mean erosion rate ($E_{cos\text{-}Qm}$), which represents the mean erosion rate over a climatic cycle,

https://doi.org/10.5194/egusphere-2026-4732
Preprint. Discussion started: 2 November 2026
© Author(s) 2026. CC BY 4.0 License.

derived from cosmogenic nuclide concentrations combined with information on climate cyclicity. We apply our model to granite catchments in the Three Rivers region of the southeastern Tibetan Plateau, where catchments experience a range of precipitation histories and climatic conditions. Using reconstructed paleo-precipitation, measured ^{10}Be concentration, and calculated channel steepness, we evaluate the potential influence of climatic precipitation cycles on erosion-rate estimates and channel steepness-erosion rate relationships.

2 Methods: Modelling framework for steepness-erosion analysis under climatic cycles

2.1 One-dimensional river longitudinal profile modelling

To investigate the relationship between channel steepness and erosion rate under climatic cycles, we conducted one-dimensional river longitudinal profile modelling. This approach allows us to track the evolution of river profiles, channel steepness metrics, and cosmogenic erosion rates in response to cyclic precipitation forcing.

Topographic change is calculated as the difference between the rock uplift rate (U) and the instantaneous fluvial erosion rate (E_{in}). Here, E_{in} represents the erosion rate at each time step, which can be predicted from the stream power law, assuming a detachment-limited fluvial system (Howard and Kerby, 1983; Howard, 1994; Whipple and Tucker, 1999):

$$E_{in} = KA^m S^n \,, \tag{1}$$

$$K = K_p P^m \,, \tag{2}$$

so that,

$$E_{in} = K_p A^m P^m S^n \,, \tag{3}$$

where K denotes erodibility accounting for precipitation effects, K_p represents erodibility without precipitation influence, S is the river slope, P is the precipitation rate, and m, n are positive components. In our 1-D river longitudinal profile modelling, we fix several parameters, including $K_p = 10^{-6}$ m$^{-0.5}$yr$^{-0.5}$, $n = 1$, and $m = 0.5$. The parameter K_p represents the erodibility that still integrates the effects of lithology and other processes, and may vary across regions (Harel et al., 2016; Haag and Schoenbohm, 2025). Because K_p primarily controls the absolute values of topographic metrics like channel steepness, while our analysis focuses on variations driven by climatic forcing, this choice does not affect the key results, and we do not investigate values of K_p. The exponent n may vary across natural systems (Lague, 2014; Harel et al., 2016). We adopt $n = 1$, as linearity simplifies the problem, although we recognize that other values of n introduce important non-linearities in results. The exponent m is chosen such that $m/n = 0.5$, a commonly observed concavity index in river profile analysis.

We also assumed a drainage area-length relationship following Hack's Law (Hack, 1957):

$$A = k_a(L - x)^h + A_c \,. \tag{4}$$

We set the river length L to 10 km for all scenarios, where x represents the distance from the outlet. The critical drainage area A_c is fixed at 1 km², with $k_a = 6.69$ and $h = 1.67$.

https://doi.org/10.5194/egusphere-2026-4732
Preprint. Discussion started: 2 November 2026
© Author(s) 2026. CC BY 4.0 License.

We consider the response of the channel profile and erosion rates to periodically changing precipitation rate, and explore various forms, periods, and amplitudes of the precipitation signal. We initialize the landscape with a flat surface and apply the stream power law under a constant uplift rate. With a cyclic precipitation function, there is an initialization period, followed by a dynamic equilibrium in which temporal variations occur only at the applied frequency, but with a phase response to specific characteristics. Once the system reaches this dynamic equilibrium, we examine the relationship between channel steepness and erosion rate. Most models have a periodic forcing, so the analysis commences once dynamic equilibrium is achieved. Our focus is on catchment-averaged erosion rates and channel steepness; therefore, all subsequent analyses are conducted at the catchment scale rather than pointwise along longitudinal river profiles.

2.2 Climate forcing models

We investigated three types of climatic forcing and their effects on channel steepness and erosion rates. We first examined the landscape response to single-frequency sinusoidal variations in precipitation and explored a range of precipitation amplitudes (P_a), mean precipitation rates (P_m), periods (T_p), and uplift rates (U). We then considered two more complex climatic forcing scenarios: an insolation-based model containing multiple periodic components and a palaeoclimate proxy record derived from $\delta^{18}O$ measurements of benthic foraminifera.

We begin with the simplest case, in which precipitation varies sinusoidally at a single frequency. The precipitation rate is prescribed as:

$$P(t) = P_a \sin\left(\frac{2\pi}{T_p} t\right) + P_m \,, \tag{5}$$

where $P(t)$ is the precipitation at time t. P_a is the amplitude of precipitation, P_m is the mean precipitation during cycles, and T_p is the period.

In addition to standard sinusoidal precipitation changes, we also considered landscape responses to an insolation-based model and a proxy-based reconstruction. These scenarios represent more general external climatic forcings, including those associated with variations in Earth's orbital parameters.

The insolation forcing represents orbitally driven climatic variability. The forcing time series was derived from astronomical calculations of July insolation at 20°N following Laskar et al. (2004). It contains multiple astronomical components with characteristic periodicities of approximately 23, 41, 100, and 405 kyr. Because the resulting signal is quasi-periodic, the model does not attain a repeating dynamic equilibrium. We applied the 10 Myr insolation record to allow transient responses to diminish, but restricted our analysis to the final tens of thousands of years, during which the model response is largely equilibrated.

The Earth system contains additional internal feedback mechanisms (e.g., ice-albedo effects) that can alter the climate away from perfect correlation with the insolation signal, so we also ran the model driven by the proxy record provided by $\delta^{18}O$ measured on benthic foraminifera (Lisiecki and Raymo, 2005; Cheng et al., 2016). Other proxies, such as loess and lake sediment records, used to infer monsoon intensity and wet-dry conditions, also exhibit patterns comparable to global benthic

https://doi.org/10.5194/egusphere-2026-4732
Preprint. Discussion started: 2 November 2026
© Author(s) 2026. CC BY 4.0 License.

foraminiferal $\delta^{18}O$ data (Ao et al., 2012). The benthic foraminiferal $\delta^{18}O$ record is characterized by a ~100 kyr component, together with the asymmetric structure of glacial cycles, marked by relatively rapid warming and more gradual cooling. We extracted the most recent 100 kyr segment and repeated it over 10 Myr to generate a periodic forcing and allow the model to reach a repeating dynamic equilibrium. Only the final 100 kyr cycle was used for analysis.

Both the insolation and benthic foraminiferal proxy records were linearly rescaled to annual precipitation while preserving their original temporal patterns. The corresponding P_a and P_m values were calculated from the most recent complete cycle of each record, where P_a is half the difference between the maximum and minimum precipitation, and P_m is the mean precipitation over the cycle. The cycle length is 23 kyr for the insolation record and 100 kyr for the benthic foraminiferal $\delta^{18}O$ record. The rationale for defining P_a and P_m in this way for insolation and proxy-based climate records is discussed in Section 5.2.

2.3 Channel steepness

To evaluate how channel steepness responds to precipitation variability, we calculated channel steepness metrics based on the stream power law.

The conventional channel steepness index k_s is defined as:

$$k_s = \left(\frac{E}{K}\right)^{\frac{1}{n}} = S \times A^{\frac{m}{n}}, \quad (6)$$

To explicitly account for precipitation, we also calculated a precipitation-modified channel steepness index $k_{s\text{-}Q}$.

$$k_{s-Q} = \left(\frac{E}{K_p}\right)^{\frac{1}{n}} = S \times (P \times A)^{\frac{m}{n}}. \quad (7)$$

From equations (3) and (7), it follows that E_{in} and $k_{s\text{-}Q}$ are proportional, assuming steady state and a uniform and constant U and K_p.

Considering temporal variations in precipitation associated with climatic cycles, we additionally calculated $k_{s\text{-}Qeff}$ following Wolpert and Schoenbohm, (2025):

$$k_{s-Qeff} = \left(\frac{E}{K_p}\right)^{\frac{1}{n}} = S \times \left(P_{eff} \times A\right)^{\frac{m}{n}}, \quad (8)$$

$$P_{eff} = \left(\frac{1}{T_p}\int_0^{T_p} P(t)^m dt\right)^{\frac{1}{m}}, \quad (9)$$

where T_p is the period of a climatic cycle, and $P(t)$ is the precipitation at time t, with t ranging from 0 to T_p.

The following analyses focus on $k_{s\text{-}Q}$ and $k_{s\text{-}Qeff}$, which explicitly account for precipitation and its temporal variability.

https://doi.org/10.5194/egusphere-2026-4732
Preprint. Discussion started: 2 November 2026
© Author(s) 2026. CC BY 4.0 License.

2.4 Cosmogenic erosion rates

Catchment-wide erosion rates are commonly inferred from concentrations of in situ cosmogenic nuclides. Although different nuclides (e.g., ^{10}Be, ^{26}Al, and ^{14}C) have different surface production rates and radioactive decay constants, the governing equations are identical. Therefore, the theoretical framework developed here is generally applicable to any cosmogenic nuclide. Unless otherwise specified, we use parameter values for ^{10}Be throughout this study, while the implications of other nuclides are discussed in Section 5.3.

2.4.1 ^{10}Be concentration

In our 1-D river longitudinal profile model, we simulate catchment-wide erosion rates derived from ^{10}Be. The concentration of ^{10}Be is calculated by integrating its production and removal over time under any given erosion history (Skov et al., 2019):

$$\frac{dN}{dt} = P_{cos}(z,t) - \lambda N(z,t)\,, \tag{10}$$

$$P_{cos}(z,t) = P_{cos-n} \times e^{-\frac{z(t)\times\rho}{\Lambda_n}} + P_{cos-ms} \times e^{-\frac{z(t)\times\rho}{\Lambda_{ms}}} + P_{cos-mf} \times e^{-\frac{z(t)\times\rho}{\Lambda_{mf}}}\,, \tag{11}$$

$$z(t) = \int_0^t E_{in}(t)dt\,, \tag{12}$$

where $P_{cos}(z, t)$ is the total production rate at depth z and time t. The subscripts n, ms and mf correspond to ^{10}Be production by nucleon spallation, slow and fast muons, respectively. Λ is the attenuation length, and ρ is the density of the material. Here we use Λ_n = 160 g/cm^2, Λ_{ms} = 1500, Λ_{mf} = 4320 g/cm^2 and ρ = 2.65 g/cm^3 (Braucher et al., 2011). We use sea-level production rates, with values set at 4, 0.012, and 0.039 at/g/yr, respectively (Braucher et al., 2011; Borchers et al., 2016). For simplicity, we neglect the effect of elevation on cosmogenic nuclide production rates. λ is the decay constant, and we use the value reported by Chmeleff et al. (2010).

$E_{in}(t)$ is the catchment-wide instantaneous erosion rate. $z(t)$ indicates that at time $t = 0$, the material is at a depth $z(t)$, and by time t, the material reaches the surface, where its depth becomes zero. For material that reaches the surface at time t, its depth at earlier times can be determined if the erosion rate history is known. Using this depth information, the production accumulation over time can be calculated. This allows us to determine the ^{10}Be concentration of the material when it reaches the surface.

2.4.2 Apparent cosmogenic erosion rate (E_{cos})

When river sand samples are collected from a catchment, the measured cosmogenic nuclide concentration (N) can be converted into an apparent erosion rate (E_{cos}). This apparent erosion rate represents the erosion rate averaged over the catchment and the timescale of cosmogenic nuclide accumulation. The relationship between cosmogenic nuclides concentration (N) and apparent erosion rate (E_{cos}) can be given as (Brown et al., 1995):

https://doi.org/10.5194/egusphere-2026-4732
Preprint. Discussion started: 2 November 2026
© Author(s) 2026. CC BY 4.0 License.

$$N = \left(\frac{P_{cos-n}}{\lambda+\frac{E_{cos}\rho}{\Lambda_n}} + \frac{P_{cos-ms}}{\lambda+\frac{E_{cos}\rho}{\Lambda_{ms}}} + \frac{P_{cos-mf}}{\lambda+\frac{E_{cos}\rho}{\Lambda_{mf}}}\right) . \quad (13)$$

Under steady-state conditions, E_{cos} is equivalent to the instantaneous erosion rate (E_{in}). When erosion rates vary through time, however, E_{cos} reflects a time-averaged erosion signal integrated over a characteristic averaging timescale. This timescale depends on the erosion rate itself, with higher erosion rates corresponding to shorter averaging timescales and lower erosion rates corresponding to longer averaging timescales. Consequently, the timescale represented by E_{cos} is not fixed and, in general, does not coincide with the duration of a climatic cycle.

2.4.3 Cosmogenic-constrained cycle-mean erosion rate ($E_{cos\text{-}Qm}$)

To estimate the mean erosion rate over a climatic cycle rather than an apparent erosion rate integrated over an erosion-rate-dependent timescale, we introduce a cosmogenic-constrained cycle-mean erosion rate ($E_{cos\text{-}Qm}$). $E_{cos\text{-}Qm}$ is defined as the mean erosion rate over one climatic cycle that is consistent with both the observed cosmogenic nuclide concentration and the prescribed precipitation history. This quantity differs from the directly measured cosmogenic erosion rate in that it takes into account the known cyclicity of the precipitation rate. This approach is particularly applicable to short-term cycles, such as those at the Milankovitch scale, where river longitudinal profiles remain relatively stable, but local erosion rates change with changing precipitation rates. Under this assumption, channel slope varies little through a climatic cycle, allowing Eq. (3) to be simplified as

$$E_{in}(t) \approx C \times P(t)^m , \quad (14)$$

where C is a scaling coefficient relating erosion rate to precipitation.

Then the depth history of a particle can be expressed as

$$z(t) = \int_0^t E_{in}(t)dt \approx \int_0^t C \times P(t)^m dt , \quad (15)$$

which allows the corresponding cosmogenic nuclide concentration to be calculated using Equations (10)-(12).

For a given precipitation history ($P(t)$), the scaling coefficient (C) is the only unknown parameter. We therefore determine the optimal value of C by minimizing the difference between the modelled cosmogenic nuclide concentration and the observed concentration using Brent's method (Brent, 2013). Brent's method combines the reliability of the golden-section search with the speed of parabolic interpolation. The algorithm iteratively brackets the minimum of a function and refines the interval using parabolic fits when the function appears smooth, ensuring both robust convergence and computational efficiency.

Once the optimal value of C is obtained, the corresponding erosion-rate history $E_{in}(t)$ can be reconstructed, and the mean erosion rate over one climatic cycle $E_{cos\text{-}Qm}$ is calculated as

$$E_{cos-Qm} = \frac{1}{T_p}\int_0^{T_p} E_{in}(t)dt . \quad (16)$$

https://doi.org/10.5194/egusphere-2026-4732
Preprint. Discussion started: 2 November 2026
© Author(s) 2026. CC BY 4.0 License.

3 Results: One-dimensional river longitudinal profile modelling

3.1 Single-frequency sinusoidal climate forcing

3.1.1 Changing P_a / P_m

We hold the uplift rate constant at 0.5 mm/yr and fix the period (T_p) at 20 kyr, varying only P_a / P_m ratios at values of 0.125, 0.25, and 0.5 (Fig. 1). For each P_a / P_m ratio, we assign two combinations of P_a and P_m (e.g., for P_a / P_m = 0.25, we use P_a = 0.1 with P_m = 0.4, and P_a = 0.3 with P_m = 1.2). This design allows us to assess how the individual values of P_a or P_m, or their ratio (P_a / P_m), influences erosion rates and channel steepness, including E_{in}, E_{cos} and $k_{s\text{-}Q}$ (Fig. 1). Although the mean values of instantaneous erosion, E_{in} and cosmogenic integrated erosion, E_{cos} remain the same, controlled by the constant uplift rate, the amplitude of E_{cos} is consistently smaller than that of E_{in} for any given P_a / P_m. Additionally, E_{cos} lags E_{in} in time, indicating a phase difference between the two. E_{cos} and $k_{s\text{-}Q}$ are also out of phase. Plotted against each other, their relationship forms an elliptical pattern rather than a straight line, illustrating the effect of this phase lag (Fig. 1d).

$E_{cos\text{-}Qm}$ and $k_{s\text{-}Qeff}$ consistently reflect the imposed uplift rate and the corresponding channel steepness across all P_a / P_m ratio scenarios and at different phases of the precipitation cycle. This indicates that both metrics serve as reliable proxies for long-term average erosion rates and channel morphology, even under conditions of substantial climatic variability (Fig. 1b-c).

A closer examination of the relationship between E_{cos} and $k_{s\text{-}Q}$ within a climatic cycle reveals that the P_a / P_m ratio is the primary factor controlling their deviation from the long-term averages, $E_{cos\text{-}Qm}$ and $k_{s\text{-}Qeff}$. When the P_a / P_m ratio is held constant, but the absolute values of P_a and P_m are varied, E_{cos} and $k_{s\text{-}Q}$ remain unchanged (Fig. 1b-c). This confirms that it is the ratio itself, not the individual values, that governs the system's response. Moreover, increasing the P_a / P_m ratio leads to greater maximum deviations of E_{cos} and $k_{s\text{-}Q}$ from their respective means, as illustrated by the enlarged ellipses in Fig. 1d. However, when $E_{cos\text{-}Qm}$ is plotted against $k_{s\text{-}Qeff}$ over a climatic cycle, nearly all cases collapse onto a single point (Fig. 1f), indicating that neither the P_a / P_m ratio nor the phase affects these metrics. This confirms that $E_{cos\text{-}Qm}$ and $k_{s\text{-}Qeff}$ reliably represent long-term averages by accounting for the effect of the sinusoidal change in precipitation rate.

https://doi.org/10.5194/egusphere-2026-4732
Preprint. Discussion started: 2 November 2026
© Author(s) 2026. CC BY 4.0 License.

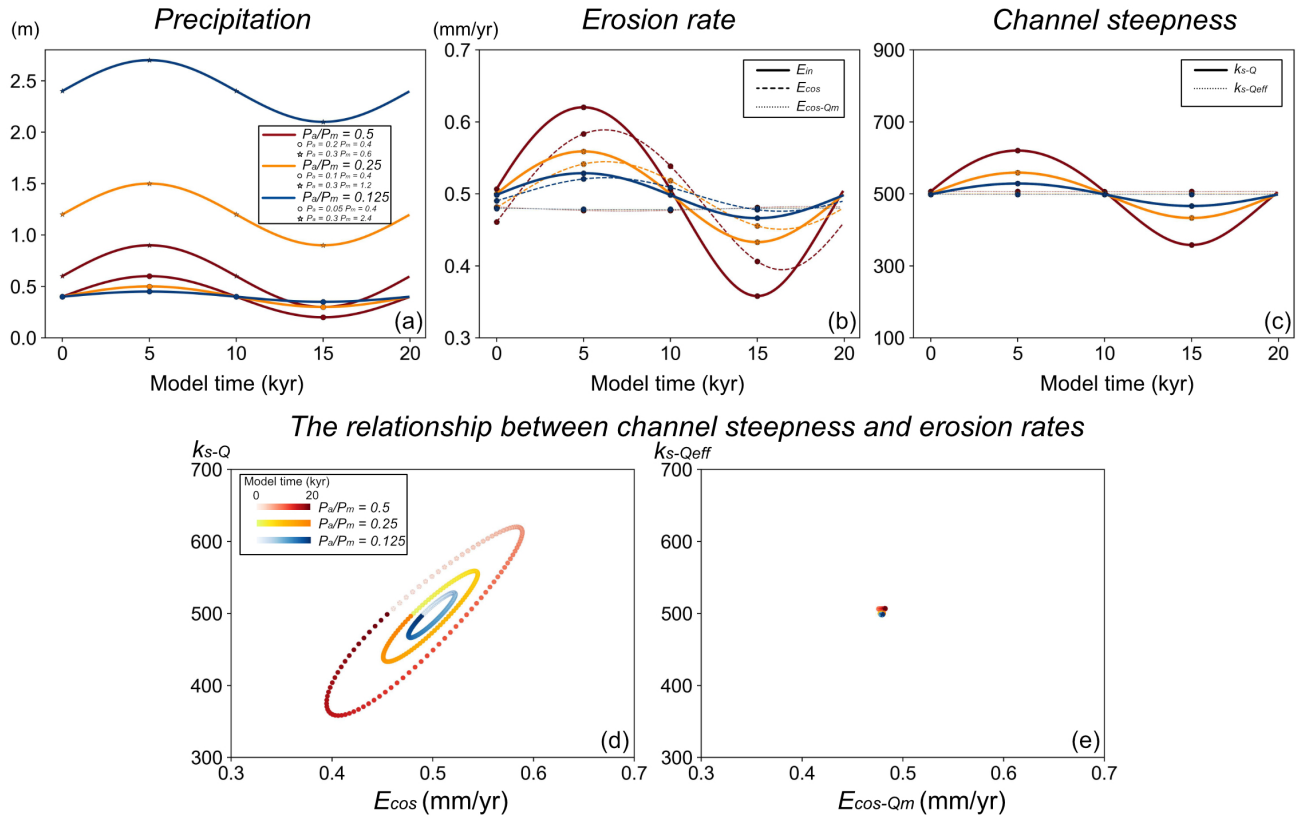


Figure 1: Catchment-averaged erosion rates and channel steepness as responses to imposed cyclic precipitation rate with different P_a / P_m. Red, yellow, and blue lines represent different P_a / P_m ratios, whereas markers indicate different absolute values of P_a and P_m. P_a and P_m are in m/yr. In panels (d) and (e), the color transition from light to dark represents the time sequence within a climatic cycle. (a) Imposed precipitation over a climatic cycle; (b) Response of erosion rates, including E_{in}, E_{cos}, and $E_{cos\text{-}Qm}$; (c) Response of channel steepness, including $k_{s\text{-}Q}$ and $k_{s\text{-}Qeff}$; (d) Relationship between erosion rate, E_{cos} and channel steepness index, $k_{s\text{-}Q}$;(e) Relationship between erosion rate parameter, $E_{cos\text{-}Qm}$ and steepness index, $k_{s\text{-}Qeff}$.

3.1.2 Changing *U*

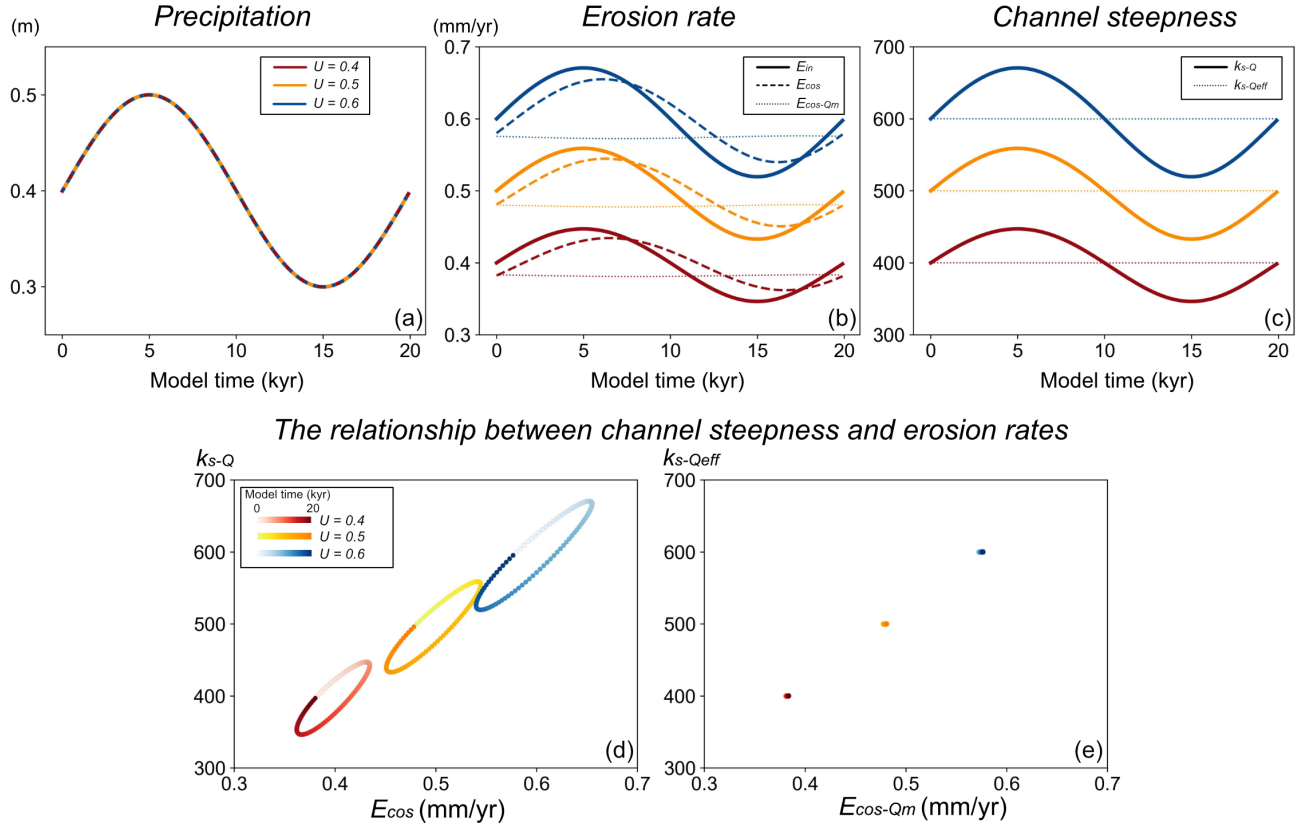
We also varied the uplift rate to 0.4, 0.5, and 0.6 mm/yr while keeping P_a / P_m fixed at 0.25. The input uplift influences the mean values of E_{in}, E_{cos} and $k_{s\text{-}Q}$ (Fig. 2). The mean values of E_{in} and E_{cos} increase with uplift rate, with higher uplift corresponding to higher mean erosion rates (Fig. 2b). Although the absolute amplitudes of E_{cos} are larger under higher uplift (Fig. 3a), their normalized amplitudes, calculated as the absolute amplitude of E_{cos} divided by $E_{cos\text{-}Qm}$, remain nearly constant across uplift scenarios, indicating that the P_a / P_m ratio continues to reflect the magnitude of the deviation (Fig. 3b). Similarly, mean $k_{s\text{-}Q}$ values increase with uplift rates (Figs. 2c, 3c), but the normalized $k_{s\text{-}Q}$ patterns, calculated as the absolute amplitude of $k_{s\text{-}Q}$ divided by $k_{s\text{-}Qeff}$, remain the same, further confirming that P_a / P_m is the dominant factor shaping variability in both erosion rates and channel steepness (Fig. 3d).

https://doi.org/10.5194/egusphere-2026-4732
Preprint. Discussion started: 2 November 2026
© Author(s) 2026. CC BY 4.0 License.

Across a climatic cycle, E_{cos} and $k_{s\text{-}Q}$ exhibit an elliptical relationship, with the center of each ellipse corresponding to the uplift rate and the corresponding $k_{s\text{-}Q}$ (Fig. 2d). When models with different uplift rates are at the same phase of the precipitation cycle, E_{cos} and $k_{s\text{-}Q}$ remain broadly proportional, with only minor variations in slope or inferred erodibility.

In contrast, when models with different uplift rates are out of phase, a model with a lower uplift rate can temporarily exhibit higher E_{cos} and $k_{s\text{-}Q}$ than a model with a higher uplift rate, particularly when the amplitudes of E_{cos} and $k_{s\text{-}Q}$ are large (Fig. 2d). For example, at the maximum precipitation phase for $U = 0.5$ mm/yr and the minimum precipitation phase for $U = 0.6$ mm/yr, the $U = 0.5$ model exhibits higher E_{cos} and $k_{s\text{-}Q}$ than the $U = 0.6$ model (Fig. 2d). This phase effect demonstrates that strong precipitation variability can temporarily obscure the expected ordering of models by uplift rate.

Plotting $E_{cos\text{-}Qm}$ against $k_{s\text{-}Qeff}$ over a climatic cycle minimizes the influence of precipitation variability and phase, and models with different uplift rates converge toward their corresponding uplift values and channel steepness (Fig. 2f). These metrics consistently reflect long-term erosion rates and channel steepness, because the modified metrics for steepness and erosion rate have been corrected for the single-period, sinusoidal variation in precipitation rate. As a result, this relationship reduces bias and maintains a consistent, linear relationship between erosion rate and channel steepness.



https://doi.org/10.5194/egusphere-2026-4732
Preprint. Discussion started: 2 November 2026
© Author(s) 2026. CC BY 4.0 License.

Figure 2: Catchment-averaged erosion rates and channel steepness as responses to imposed cyclic precipitation rate with different *U*. *U* is in mm/yr. In panels (d) and (e), the color transition from light to dark represents the time sequence within a climatic cycle. (a) Imposed precipitation over a climatic cycle; (b) Response of erosion rates, including E_{in}, $E_{cos,}$ and $E_{cos\text{-}Qm}$; (c) Response of channel steepness, including $k_{s\text{-}Q}$ and $k_{s\text{-}Qeff}$; (d) Relationship between erosion rate, E_{cos} and channel steepness index, $k_{s\text{-}Q}$;(e) Relationship between erosion rate parameter, $E_{cos\text{-}Qm}$ and steepness index, $k_{s\text{-}Qeff}$.

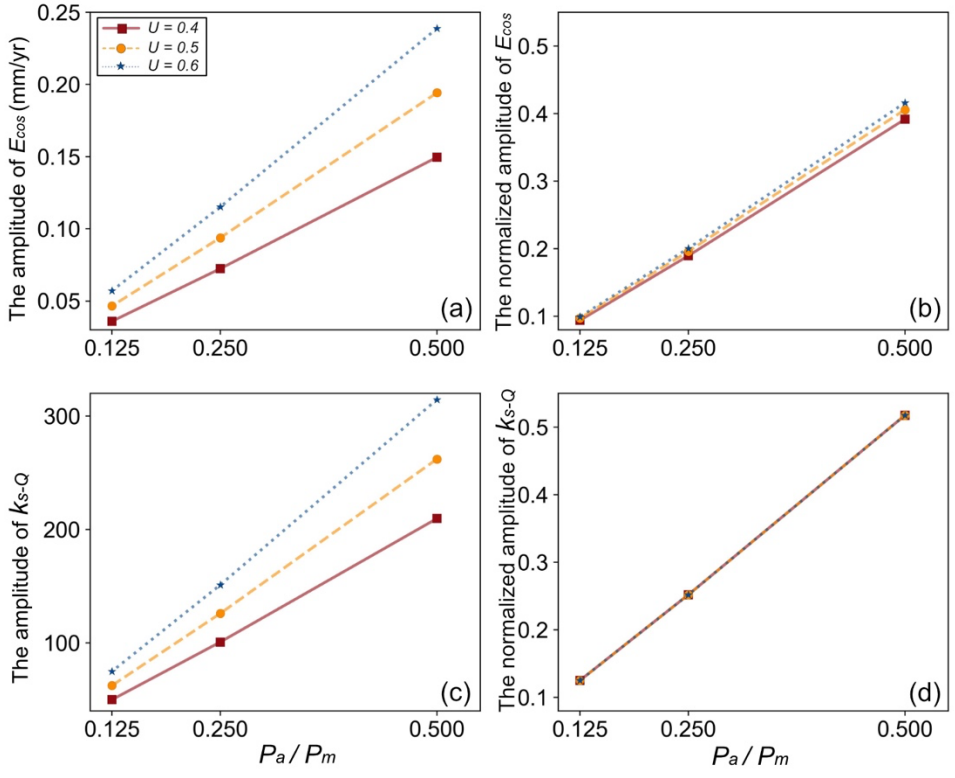


Figure 3: Influence of P_a / P_m ratio and *U* on the amplitude of E_{cos} and $k_{s\text{-}Q}$. Markers and colors represent *U*, corresponding to the individual model runs. *U* is in mm/yr. Lines indicate variation in amplitude with P_a / P_m. (a) Amplitude of E_{cos}; (b) Normalized amplitude of E_{cos}, calculated as the amplitude of E_{cos} divided by $E_{cos\text{-}Qm}$; (c) Amplitude of $k_{s\text{-}Q}$; (d) Normalized amplitude of $k_{s\text{-}Q}$, calculated as the amplitude of $k_{s\text{-}Q}$ divided by $k_{s\text{-}Qeff}$.

3.1.3 Changing the period of precipitation (T_p)

The relative difference between the climatic cycle period and the timescale of cosmogenic nuclides is an important characteristic of the system. To assess this, we examine the influence of precipitation period (T_p) on river profiles with fixed values of P_a / P_m = 0.25 and U = 0.5 mm/yr. The selected T_p values for analysis are 1000 kyr, 100 kyr, 20 kyr, and 2 kyr. The results presented here are based on parameter values for ^{10}Be, while the implications for other cosmogenic nuclides are covered in the Discussion. When the climatic cycle is very long (e.g., T_p = 1000 kyr), E_{cos} closely follows the instantaneous erosion rate (E_{in}) (Fig. 4a). In contrast, when T_p is short (e.g., T_p = 2 kyr), E_{cos} already reflects the long-term average erosion

https://doi.org/10.5194/egusphere-2026-4732
Preprint. Discussion started: 2 November 2026
© Author(s) 2026. CC BY 4.0 License.

rate, making further averaging like $E_{cos\text{-}Qm}$ unnecessary. For intermediate periods such as those on Milankovitch timescales (T_p = 100 kyr, 20 kyr), a noticeable lag and amplitude difference emerge between E_{cos} and E_{in}, highlighting the need to calculate $E_{cos\text{-}Qm}$ to accurately represent long-term erosion rates.

Similarly, channel steepness patterns respond differently depending on T_p. When the period is long (e.g., T_p = 1000 kyr), slope continues to vary over time, causing $k_{s\text{-}Qeff}$ to oscillate (Fig. 4b). In contrast, for Milankovitch-scale or shorter cycles (T_p = 100 kyr, 20 kyr, and 2 kyr), $k_{s\text{-}Qeff}$ remains relatively stable over time. This suggests that river profiles undergo greater adjustment under longer climatic cycles (Goren, 2016), whereas over shorter, Milankovitch-scale cycles, the relative stability of channel geometry allows $E_{cos\text{-}Qm}$ and $k_{s\text{-}Qeff}$ to provide robust measures of long-term erosion and channel steepness.

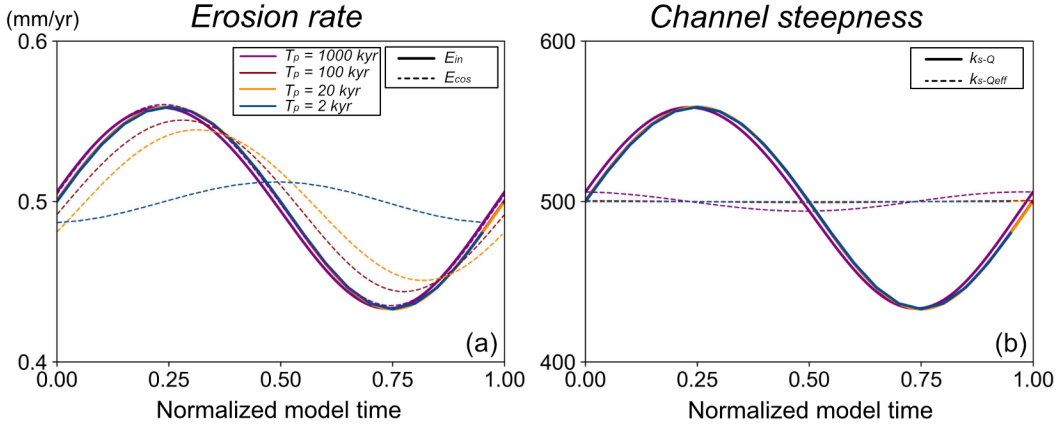


Figure 4: Catchment-averaged erosion rates and channel steepness with changing period, T_p. Normalized model time is calculated by dividing model time by T_p. (a) E_{in} and E_{cos}; (b) $k_{s\text{-}Q}$ and $k_{s\text{-}Qeff}$.

3.2 Insolation and proxy-based climate forcing

Here we present the response to precipitation cycles driven by a model of northern hemisphere insolation with multifrequency and by an empirical global compilation of $\delta^{18}O$ in benthic foraminifera (Figs. 5-6).

3.2.1 Insolation forcing

For the precipitation cycle scaled from a theoretical insolation time series, the uplift rate is fixed at 0.5 mm/yr, and only P_a / P_m is varied, with values of 0.16, 0.08, and 0.04 (Fig. 5). The same patterns observed for the sinusoidal cycles (Figs. 1) are also evident in in Fig. 5: as P_a / P_m increases, the maximum deviations of E_{in}, E_{cos}, and $k_{s\text{-}Q}$ from their mean values become larger (Fig. 5b-d). In contrast, $E_{cos\text{-}Qm}$ and $k_{s\text{-}Qeff}$ recover the imposed uplift rate and the corresponding channel steepness (Fig. 5e). Compared with the sinusoidal precipitation cycles (Fig. 1), the insolation-scaled precipitation cycles have smaller P_a / P_m values and show correspondingly smaller amplitudes in E_{in}, E_{cos}, and $k_{s\text{-}Q}$ (Fig. 5).

https://doi.org/10.5194/egusphere-2026-4732
Preprint. Discussion started: 2 November 2026
© Author(s) 2026. CC BY 4.0 License.

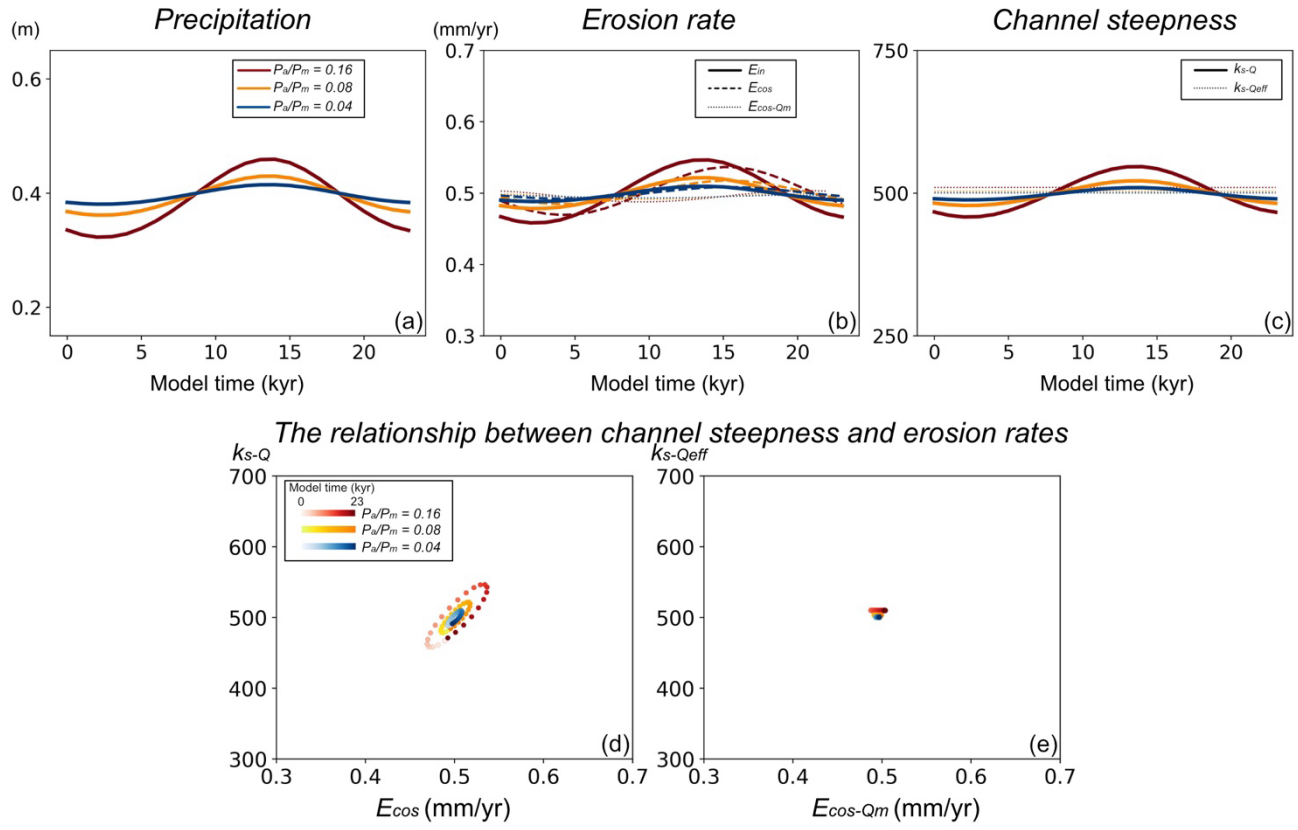


Figure 5: Catchment-averaged erosion rates and channel steepness in response to the precipitation cycle scaled from a theoretical insolation time series. Red, yellow, and blue lines represent different P_a / P_m ratios. P_a and P_m are in m/yr. In panels (d) and (e), the color transition from light to dark represents the time sequence within a climatic cycle. (a) Precipitation over a climatic cycle; (b) E_{in}, E_{cos}, and $E_{cos\text{-}Qm}$; (c) $k_{s\text{-}Q}$ and $k_{s\text{-}Qeff}$; (d) E_{cos} versus $k_{s\text{-}Q}$;(e) $E_{cos\text{-}Qm}$ versus $k_{s\text{-}Qeff}$.

3.2.2 Proxy-based climate forcing

For the model including the precipitation cycle scaled from the global benthic foraminiferal $\delta^{18}O$ record, the uplift rate is fixed at 0.5 mm/yr, and only P_a / P_m is varied, with values of 0.125, 0.25, and 0.5 (Fig. 6). The amplitude of E_{cos} consistently remains smaller than that of E_{in}. E_{cos} lags behind E_{in} and is also out of phase with $k_{s\text{-}Q}$. Although E_{cos} and $k_{s\text{-}Q}$ no longer form a perfect elliptical pattern, their relationship remains approximately elliptical (Fig. 6d). P_a / P_m still remains the primary control on the amplitude of E_{cos} and $k_{s\text{-}Q}$, consistent with results from sinusoidal cycles and cycles scaled from the insolation model. As P_a / P_m increases, their maximum deviations from the mean grow larger, producing broader ellipses in Fig. 6d. Despite this variability, $E_{cos\text{-}Qm}$ and $k_{s\text{-}Qeff}$ still capture the imposed uplift rate and the corresponding channel steepness across all P_a / P_m values and phases of the benthic cycle, though the spread of $E_{cos\text{-}Qm}$ is wider under the empirical forcing function compared to the perfect sinusoidal forcing.

https://doi.org/10.5194/egusphere-2026-4732
Preprint. Discussion started: 2 November 2026
© Author(s) 2026. CC BY 4.0 License.

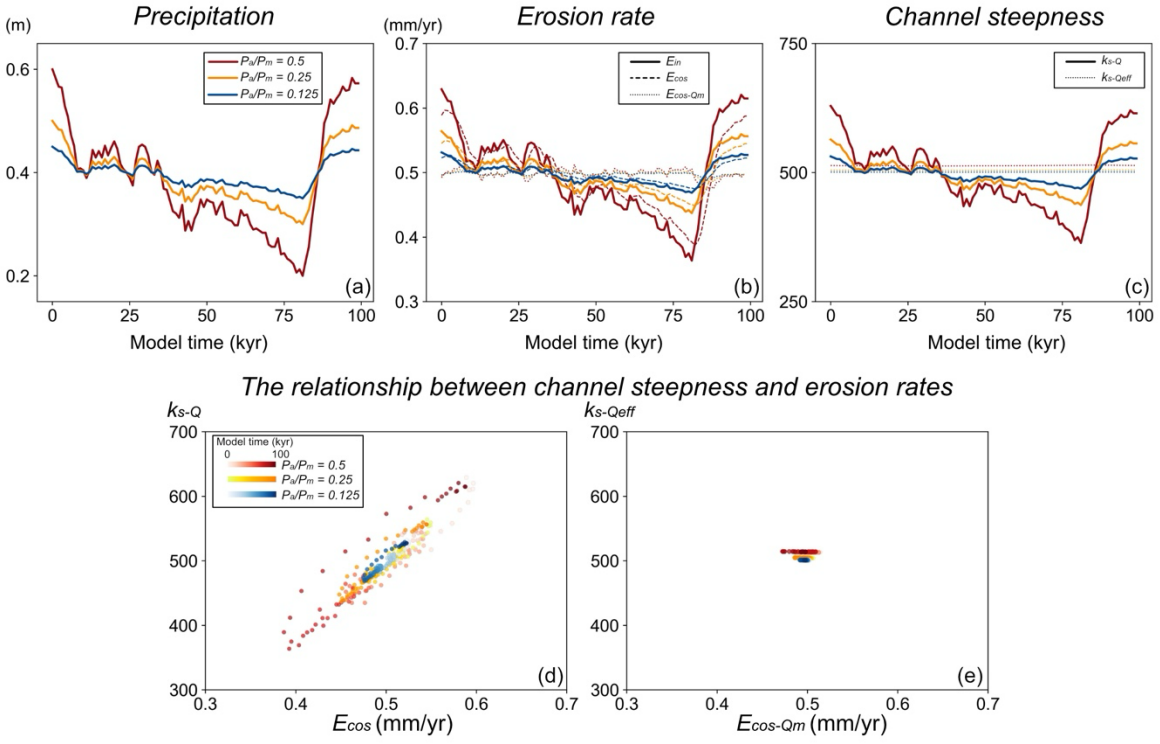


Figure 6: Catchment-averaged erosion rates and channel steepness in response to the precipitation cycle scaled from the global benthic foraminiferal $\delta^{18}O$ record. Red, yellow, and blue lines represent different P_a / P_m ratios. P_a and P_m are in m/yr. In panels (d) and (e), the color transition from light to dark represents the time sequence within a climatic cycle. (a) Precipitation over a climatic cycle; (b) E_{in}, $E_{cos,}$ and E_{cos-Qm}; (c) k_{s-Q} and k_{s-Qeff}; (d) E_{cos} versus k_{s-Q}; (e) E_{cos-Qm} versus k_{s-Qeff}.

4 Case Study of regional data from the Three Rivers Region

4.1 Characterizing precipitation cycles, channel steepness, and erosion

We selected the Three Rivers Region (TRR, Fig. 7a) as a case study to examine how spatial and temporal variations in precipitation influence the relationship between channel steepness and erosion rate. The region is well suited for this purpose because it spans a broad precipitation gradient and contains many catchment-wide ^{10}Be erosion-rate measurements.

Precipitation varies markedly across the TRR. The southern part of the region generally receives more rainfall, likely influenced by the Indian Summer Monsoon, while the northern portion, situated on the Tibetan Plateau, tends to be much drier. Temporal precipitation variability may also differ between these areas. Ao et al. (2012) suggested that North China monsoon records broadly follow the 100 kyr glacial–interglacial cycle, possibly because the summer monsoon reached the region mainly during interglacials and may not have reached it during glacials. In contrast, South China remained under monsoon influence and responded more directly to the 23 kyr insolation cycle. Although direct palaeoclimate records from

https://doi.org/10.5194/egusphere-2026-4732
Preprint. Discussion started: 2 November 2026
© Author(s) 2026. CC BY 4.0 License.

within the TRR are limited, nearby proxy records are broadly consistent with this possibility. Stalagmite records from Xiaobailong Cave in southwestern China, close to the southern TRR, suggest long-term fluctuations in precipitation over the past 252 kyr that broadly correspond to orbital insolation cycles (Cai et al., 2015). Similar cyclic variations have also been reported from southeastern China (Wang et al., 2001; Dykoski et al., 2005). In contrast, proxy records from the Tibetan Plateau suggest that conditions during the Last Glacial Maximum (LGM) were much drier than at present (Wang et al., 2002; Kotlia et al., 2010; Hu et al., 2014). Climate-model simulations also indicate possible north–south differences within the TRR in precipitation changes between the LGM and the present (Li et al., 2017; Mutz et al., 2018; Kageyama et al., 2021). These palaeoclimate records provide regional context for the possible dominant timescales of precipitation variability, but were not used directly to reconstruct catchment-specific precipitation histories.

We selected catchments from both the southern and northern TRR for which catchment-wide ^{10}Be measurements were available. To minimize the influence of lithology on erodibility, we selected catchments predominantly underlain by granitic basement. The dataset comprises 25 catchments with measured cosmogenic ^{10}Be concentrations, including 20 catchments from tributaries of the Salween River, 3 from tributaries of the Yuqu River (the largest tributary of the Salween River), and 2 from tributaries of the Mekong River, compiled from Fang et al. (2026) and Henck et al. (2011) (Fig. 7a, Table 1).

Catchment-specific precipitation histories were derived from the CHELSA-TraCE21k dataset, which provides precipitation estimates from the present to the Last Glacial Maximum (LGM, ~21 ka) at 100-year intervals (Karger et al., 2021). The simulated precipitation patterns are generally comparable to those inferred from nearby stalagmite and proxy records. Precipitation time series were extracted for each catchment, and catchment-averaged precipitation was calculated at each time step to characterize temporal variations (Fig. 7) and identify the timing of minimum precipitation and maximum precipitation. To reconstruct complete precipitation cycles for each catchment, we applied different approaches to the northern and southern data, reflecting the different periods of temporal climate variation (Fig. 7). For basins in the south, dominated by the precessional monsoon cycles, precipitation histories were fit using the insolation model. For basins in the north, where precipitation is dominated by the 100 kyr cycle and a different phase with minimum precipitation lagging the LGM, the benthic foraminifera δ^{18}O proxy record was used. In both cases, precipitation was fit using linear least-squares regression by minimizing the squared differences between CHELSA-TraCE21k precipitation and either the insolation model or proxy-based predictions. This approach allows us to extend the precipitation histories beyond the range provided by the CHELSA-TraCE21k model, which only covers the period from the Last Glacial Maximum (~21 ka) to the present. Based on the fitted precipitation time series, we calculated the amplitude of the dominant precipitation cycle (P_a), the mean precipitation (P_m), and their ratio (P_a / P_m) (Fig. 8). Consistent with the 1-D river-model experiments, these metrics were calculated over the most recent representative cycle: the final 23 kyr for the insolation forcing and the final 100 kyr for the benthic δ^{18}O -based forcing. This approach implicitly assumes that mean precipitation (P_m) remains approximately constant through time. While this assumption may not fully reflect natural variability, it provides a simplified framework for quantifying effects of the higher-frequency cyclicity. The implications of this assumption are further discussed in Section 5.3.

https://doi.org/10.5194/egusphere-2026-4732
Preprint. Discussion started: 2 November 2026
© Author(s) 2026. CC BY 4.0 License.

With reconstructed precipitation cycles, we can calculate $E_{cos\text{-}Qm}$ and $k_{s\text{-}Qeff}$, and compare them to the original metrics E_{cos} and $k_{s\text{-}Q}$. E_{cos} values are calculated following the formulation of Brown et al. (1995). Surface production rates are derived from sea-level high-latitude (SLHL) reference values (Braucher et al., 2011) and scaled by latitude and elevation using the scaling parameters of Stone (2000). Elevation data are obtained from the GLO-DEM, and catchment-averaged production rates are used for calculations. Apparent erosion rates (E_{cos}) are then estimated under the assumption of a constant erosion history. $E_{cos\text{-}Qm}$ is computed using Equations (14)-(16), incorporating the full fitted precipitation cycles, while applying the same surface production parameters as in the E_{cos} calculation. We adapt a reference concavity index of m/n = 0.5 and compute the normalized channel steepness indices $k_{sn\text{-}Q}$ and $k_{sn\text{-}Qeff}$. The $k_{sn\text{-}Q}$ values are calculated using modern (0 ka) precipitation from the CHELSA-TraCE21k model. $k_{sn\text{-}Qeff}$ values are calculated using P_m from the fitted precipitation cycles, thereby accounting for the influence of long-term climate variability.

4.2 Patterns of precipitation cycles, channel steepness, and erosion

Catchment-averaged precipitation time series and the ages of minimum precipitation are shown in Fig. 7. In the northern catchments, minimum precipitation occurred earlier, typically near 20 ka, indicating that the LGM was drier than present (Fig. 7a). In contrast, the southern catchments show minimum precipitation around 15 ka, following the LGM, with precipitation rates during the LGM variable, but often similar to modern. When examined individually, catchments 1 to 20, located south of 28°N, generally experienced higher precipitation during at least part of the LGM, with minimum precipitation occurring around 15 ka (Fig. 7b), consistent with regional stalagmite records (Fig. 7c). In comparison, catchments 21 to 25, north of 28°N, had lower precipitation during the LGM, with minimum values around 20 ka, aligning more closely with the $\delta^{18}O$ proxy records (Fig. 7d).

https://doi.org/10.5194/egusphere-2026-4732
Preprint. Discussion started: 2 November 2026
© Author(s) 2026. CC BY 4.0 License.

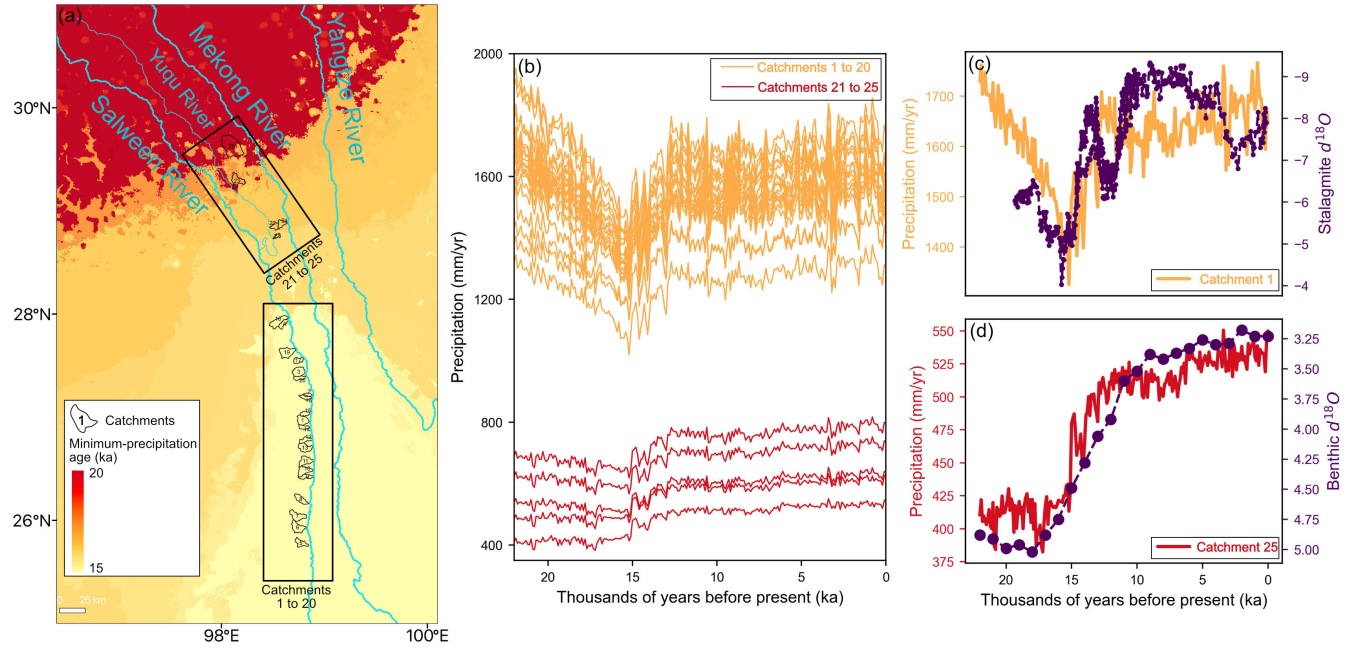
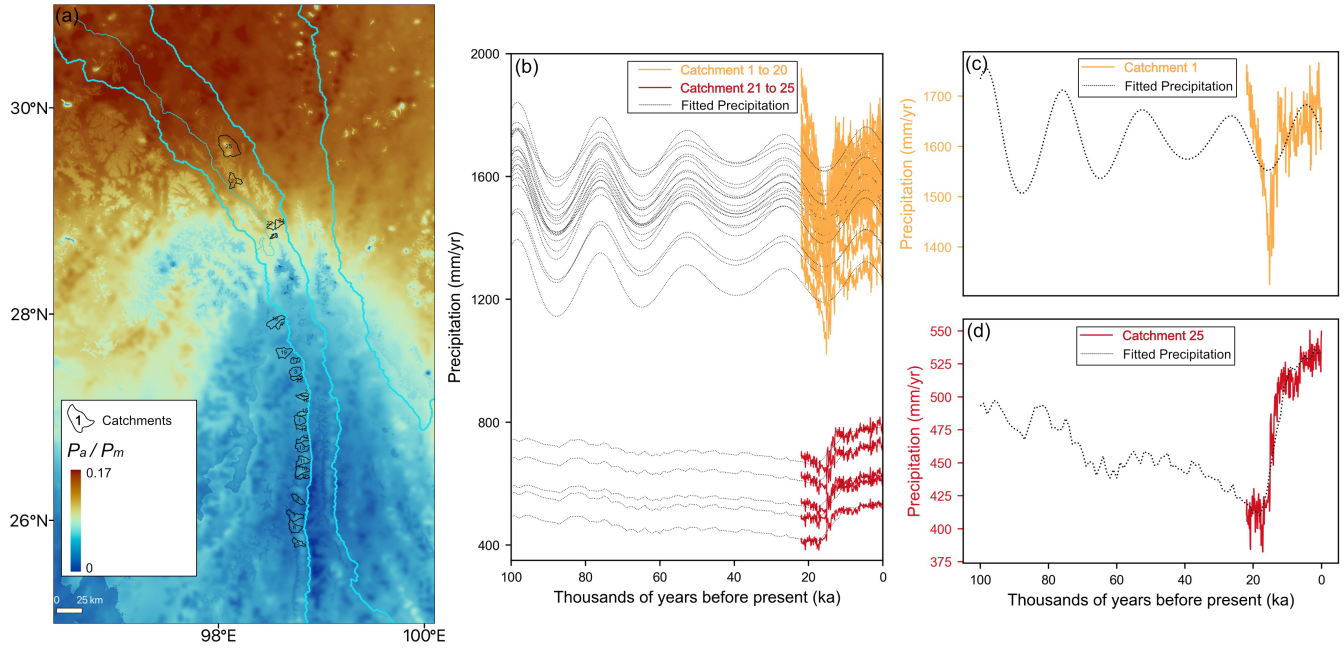


Figure 7: Minimum-precipitation age and catchment-averaged precipitation (21 ka to present) for granite catchments in the Three Rivers region, based on the CHELSA TraCE21k climate model (Karger et al., 2021). (a) Age of minimum precipitation between 21 ka and the present; (b) Catchment-averaged precipitation from 21 ka to present for all catchments; (c) Precipitation time series for Catchment 1 compared with stalagmite δ¹⁸O records from southeastern China (Wang et al., 2001; Dykoski et al., 2005); (d) Precipitation time series for Catchment 25 compared with the global benthic foraminifera δ¹⁸O record (Lisiecki and Raymo, 2005).

Fig. 8a presents the spatial distribution of the ratio P_a / P_m. The map reveals a clear spatial pattern: catchments in the southern TRR generally exhibit low P_a / P_m values, all below 0.1, while northern catchments display higher ratios, ranging from 0.1 to 0.17. Fig. 8b-d display the fitted precipitation curves for all 25 catchments. These curves closely align with the CHELSA-TraCE21k model outputs, supporting the validity of the fitted reconstructions.

https://doi.org/10.5194/egusphere-2026-4732
Preprint. Discussion started: 2 November 2026
© Author(s) 2026. CC BY 4.0 License.



405 **Figure 8: P_a / P_m ratios and fitted precipitation histories for all granite catchments in the Three Rivers region. In panels (b)-(d), red and yellow lines represent precipitation from the CHELSA TraCE21k model (Karger et al., 2021), while black dashed lines show fitted precipitation curves based on orbital insolation and global benthic foraminifera $\delta^{18}O$ records. (a) P_a / P_m; (b) Precipitation time series (21 ka to present) for all granite catchments; (c) Precipitation for Catchment 1; (d) Precipitation for Catchment 25.**

410 Table 1 and Fig. 9 present the comparisons between E_{cos} and $k_{sn\text{-}Q}$, as well as $E_{cos\text{-}Qm}$ and $k_{sn\text{-}Qeff}$. Overall, the differences between the paired metrics are modest across all catchments, and the regression performance does not improve significantly when using $E_{cos\text{-}Qm}$ and $k_{sn\text{-}Qeff}$ instead of E_{cos} and $k_{sn\text{-}Q}$. This limited improvement may reflect the relatively small P_a / P_m ratios in many catchments. However, a clearer distinction emerges when considering the relative differences. In catchments 21-25, which have higher P_a / P_m values, $k_{sn\text{-}Q}$ deviates from $k_{sn\text{-}Qeff}$ by approximately 5-10%, and E_{cos} deviates from $E_{cos\text{-}Qm}$
415 by about 10-20%. In contrast, catchments 1-20, which have lower P_a / P_m , show much smaller deviations, around 0-5% for $k_{sn\text{-}Q}$ and up to 5% for E_{cos}.

https://doi.org/10.5194/egusphere-2026-4732
Preprint. Discussion started: 2 November 2026
© Author(s) 2026. CC BY 4.0 License.

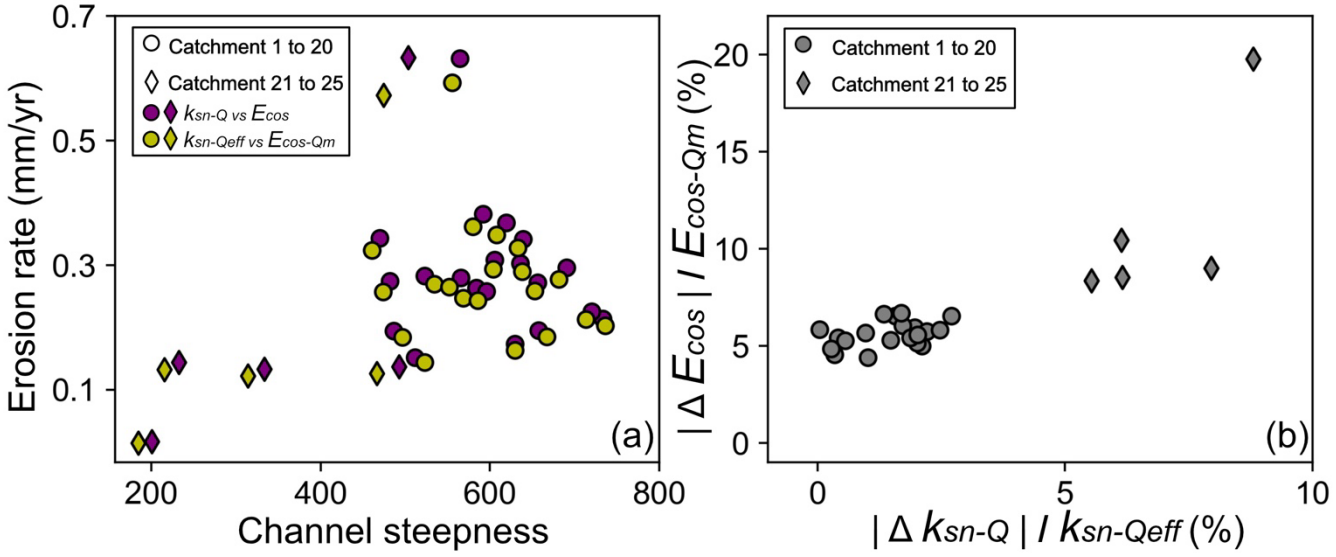


Figure 9: Relationship between channel steepness and erosion rates. (a) Comparison of E_{cos} versus k_{sn-Q} and E_{cos-Qm} versus $k_{sn-Qeff}$; (b) Relative differences between E_{cos} and E_{cos-Qm}, and k_{sn-Q} and $k_{sn-Qeff}$.

Table 1: Catchment information

No.	Sample	Lat (ºN)	Lon (ºE)	^{10}Be (at/g)	^{10}Be 1σ(%)	E_{cos} (mm/yr)	k_{sn-Q}	E_{cos-Qm} (mm/yr)	$k_{sn-Qeff}$
1	NUJ15-06	26.9698	98.7878	47557	4.9	0.342	639	0.328	633
2	NUJ15-07	27.2166	98.8371	38497	5.3	0.343	470	0.324	461
3	NUJ15-08	27.44	98.7495	26044	5.6	0.632	564	0.593	556
4	NUJ15-10	27.9042	98.5985	79649	4.3	0.263	584	0.247	569
5	NJ-3-L23	25.7492	98.8447	86319	5.2	0.152	511	0.144	523
6	NJ-4-L26	25.9303	98.8246	44818	5.6	0.283	523	0.27	534
7	NJ-5-L29	26.0302	98.8247	78594	4.5	0.194	487	0.184	497
8	NJ-7-L33	26.1657	98.8469	85740	3.9	0.195	658	0.185	667
9	NJ-10-L38	26.4254	98.8916	72917	3.8	0.214	733	0.203	736
10	NJ-12-L40	26.489	98.8913	52548	4.3	0.303	636	0.29	638
11	NJ-13-L42	26.5801	98.8993	94158	3.5	0.173	630	0.163	630
12	NJ-16-L48	26.7837	98.8836	60909	3.7	0.272	656	0.258	653
13	NJ-17-L45	26.7161	98.8905	53373	4.4	0.308	606	0.294	604
14	NJ-20-L51	26.9007	98.856	70350	3.8	0.225	720	0.213	713

https://doi.org/10.5194/egusphere-2026-4732
Preprint. Discussion started: 2 November 2026
© Author(s) 2026. CC BY 4.0 License.

15	NJ-21-L54	27.0356	98.8599	52879	4	0.296	691	0.278	682
16	NJ-23-L57	27.1864	98.878	61976	3.8	0.258	596	0.243	586
17	NJ-27-L66	27.5773	98.7879	46064	5.5	0.368	619	0.349	608
18	NJ-30-L76	27.9662	98.6583	77914	4	0.28	566	0.265	552
19	NJ-37-L68	27.6618	98.7151	47945	5.6	0.382	592	0.362	580
20	NJ-38-L63	27.4044	98.826	62411	4.6	0.274	482	0.257	474
21	Yuqu-3-E7	28.7309	98.4993	261453	2.1	0.137	493	0.126	467
22	Yuqu-5-E9	28.8378	98.4702	261194	2.7	0.133	333	0.123	314
23	Yuqu-6-E21	29.2154	98.1048	303266	2.4	0.144	233	0.132	216
24	LCJ-19-W83	28.8822	98.6386	52705	4.6	0.633	503	0.573	474
25	43-Mek	29.55	98.21	2768030	2.4	0.017	201	0.014	185

* ^{10}Be data for entries 1–24 are from Fang et al. (2026); data for entry 25 are from Henck et al. (2011).

5 Discussion and Limitations

5.1 Applicability of 1-D river modelling

In this study, we employ a 1-D river profile model that assumes spatially uniform precipitation with temporal variability. Previous work has highlighted that spatially variable precipitation, such as top-heavy or bottom-heavy rainfall gradients, can exert important controls on river response, particularly when considering drainage networks that include both large trunks and relatively small tributaries (Leonard and Whipple, 2021; Wolpert and Schoenbohm, 2025). One-dimensional river profile modelling work of both trunk and tributaries (Leonard and Whipple, 2021) shows that tributaries typically experience a relatively muted range in precipitation due to their orientation and smaller areal extent, whereas large trunk rivers may integrate spatial precipitation gradients. At the same time, tributary evolution is influenced both by local climatic forcing and by base-level changes imposed by the trunk river. Two-dimensional landscape evolution models (Wolpert and Schoenbohm, 2025) also demonstrate that, under spatially variable precipitation, trunk and tributary systems can exhibit discordance at confluences. This arises because trunk rivers integrate upstream-averaged runoff, while tributaries remain more closely attuned to local conditions.

Although 2-D landscape evolution modelling can provide more information for complex river network systems, 1-D river profile modelling is sufficient for our primary focus, which is the relationship between channel steepness and cosmogenic erosion rates. This relationship is typically applied to relatively small and comparable catchments that do not integrate overly complex spatial variations in climate and tectonics, such as small tributaries in the TRR. The focus of this study is not to compare responses between trunk and tributary systems, but rather to isolate the effects of temporal changes in precipitation on the relationship between channel steepness and erosion rates. Under these conditions, a 1-D framework that assumes

https://doi.org/10.5194/egusphere-2026-4732
Preprint. Discussion started: 2 November 2026
© Author(s) 2026. CC BY 4.0 License.

spatially uniform forcing within individual catchments provides a simplified yet appropriate representation of the dominant processes. By avoiding additional complexities, this approach yields clearer and more intuitive results, allowing us to directly evaluate how temporal variability alone can bias geomorphic metrics. These results also provide a useful basis for interpreting more complex 2-D models and natural systems.

5.2 P_a / P_m controls and its calculation in proxy-based precipitation cycles

The model results and case studies of this paper (Figs. 1, 8, 9) show that the ratio of precipitation amplitude to mean precipitation (P_a / P_m) is a key factor controlling the deviation of E_{cos} and $k_{s\text{-}Q}$ from long-term erosion rates and the corresponding channel steepness value. This conclusion is supported by theoretical analysis of the governing equations.

For instantaneous erosion rate (E_{in}), the normalized amplitude of erosion rate fluctuations (ΔE_{in}), assuming channel slope remains constant, can be approximated by:

$$\Delta E_{in} = \frac{E_{in-max} - E_{in-mean}}{E_{in-mean}} = \frac{K_p S^n \times (P_{max} \times A)^m - K_p (S_m)^n \times (P_{mean} \times A)^m}{K_p (S_m)^n \times (P_{mean} \times A)^m}$$

$$\approx \frac{(P_a + P_m)^m - (P_m)^m}{(P_m)^m} \approx \left(\frac{P_a}{P_m} + 1\right)^m - 1 \,. \quad (17)$$

Similarly, for precipitation-modified channel steepness ($k_{s\text{-}Q}$), the normalized amplitude (Δk_{s-Q}) can be expressed as:

$$\Delta k_{s-Q} = \frac{K_{spmax} - K_{spmean}}{K_{spmean}} = \frac{S \times (P_{max} \times A)^{\frac{m}{n}} - S_m \times (P_{mean} \times A)^{\frac{m}{n}}}{S_m \times (P_{mean} \times A)^{\frac{m}{n}}}$$

$$\approx \frac{(P_a + P_m)^{\frac{m}{n}} - (P_m)^{\frac{m}{n}}}{(P_m)^{\frac{m}{n}}} \approx \left(\frac{P_a}{P_m} + 1\right)^{\frac{m}{n}} - 1 \,. \quad (18)$$

Equations (17) and (18) show that the normalized amplitudes of both E_{in} and $k_{s\text{-}Q}$ are directly controlled by P_a / P_m, assuming constant concavity. Since E_{cos} reflects the integrated behavior of E_{in}, its variability is also governed by P_a / P_m. However, due to the averaging timescale inherent in cosmogenic erosion rates, the period of the climatic cycle (T_p) can also influence E_{cos}. When considering the absolute amplitudes of E_{cos} and $k_{s\text{-}Q}$, their mean values, primarily controlled by the uplift rates, also become important factors.

Model results, case studies (Figs. 1, 8, 9), and theoretical analysis (Equations 17 and 18) demonstrate P_a / P_m is a key factor in determining whether it is necessary to calculate $E_{cos\text{-}Qm}$ and $k_{sn\text{-}Qeff}$. When P_a / P_m is low, the amplitudes of E_{cos} and $k_{sn\text{-}Q}$ are minimal (Fig. 1, e.g., P_a / P_m =0.2), and the differences between E_{cos} and $E_{cos\text{-}Qm}$ or between $k_{sn\text{-}Q}$ and $k_{sn\text{-}Qeff}$ across catchments 1 to 20 (Figs. 8, 9) are also negligible. In contrast, when P_a / P_m is high, the differences become substantial. For instance, when P_a / P_m reaches 0.5, the deviation between E_{cos} and $E_{cos\text{-}Qm}$, or between $k_{sn\text{-}Q}$ and $k_{sn\text{-}Qeff}$, can reach ~30% (Fig. 1b-e). Under these conditions, accounting for long-term precipitation variability is essential for accurately interpreting the relationship between erosion rates and channel steepness.

The timing, or phase, of the precipitation cycle further influences the analysis. Catchments 21 to 25, for example, appear to be in a phase of maximum precipitation, likely driven by dominant 100 kyr cycles. As a result, they correspond to the peak

https://doi.org/10.5194/egusphere-2026-4732
Preprint. Discussion started: 2 November 2026
© Author(s) 2026. CC BY 4.0 License.

values of E_{cos} and $k_{sn\text{-}Q}$. Catchments 1 to 20 are more complex; the dominant cycles are likely around 23 kyr, and present-day precipitation is lower than during the early parts of the Last Glacial Maximum. This difference in both cycle period and phase introduces additional variability. Fortunately, the P_a / P_m values for these catchments are low, which helps mitigate the influence of phase differences. However, if P_a / P_m were higher, these catchments would not coincide with a peak precipitation phase, potentially reversing the relationship between E_{cos} and $k_{sn\text{-}Q}$, compared to the corrected results, $E_{cos\text{-}Qm}$ and $k_{sn\text{-}Qeff}$ (Fig. 2).

A further issue is how P_a / P_m should be calculated for proxy-based precipitation cycles and natural climatic variability, where multiple periodicities may coexist, and both precipitation amplitude and mean precipitation can vary through time. The calculation of P_a / P_m in our model and case study is based on the most recent cycle, but also on what we interpret as the dominant period. This choice is supported by the temporal evolution of cosmogenic nuclide production rates before the present under a range of erosion rates (Fig. 10). Using ^{10}Be parameters and surface production rates derived from sea-level high-latitude (SLHL) reference values (Braucher et al., 2011), we evaluate the effective integration timescale of the signal. For example, at an erosion rate of 0.1 mm/yr, the production remains significant only over the most recent ~20 ka and becomes negligible by ~40 ka. For higher erosion rates (0.5 mm/yr and above), the effective record length is even shorter, typically less than 20 ka. Only at very low erosion rates (e.g., 0.01 mm/yr) do longer-term production-rate variations exert a substantial influence.

Therefore, although P_a and P_m may vary through time in principle, for typical erosion rates in tectonically active settings (generally $\geq$ 0.1 mm/yr), only the most recent part of the production history contributes meaningfully to the measured signal. Under these conditions, it is reasonable to calculate P_a / P_m using the most recent cycle and to limit the reconstruction period to 100 ka.

https://doi.org/10.5194/egusphere-2026-4732
Preprint. Discussion started: 2 November 2026
© Author(s) 2026. CC BY 4.0 License.

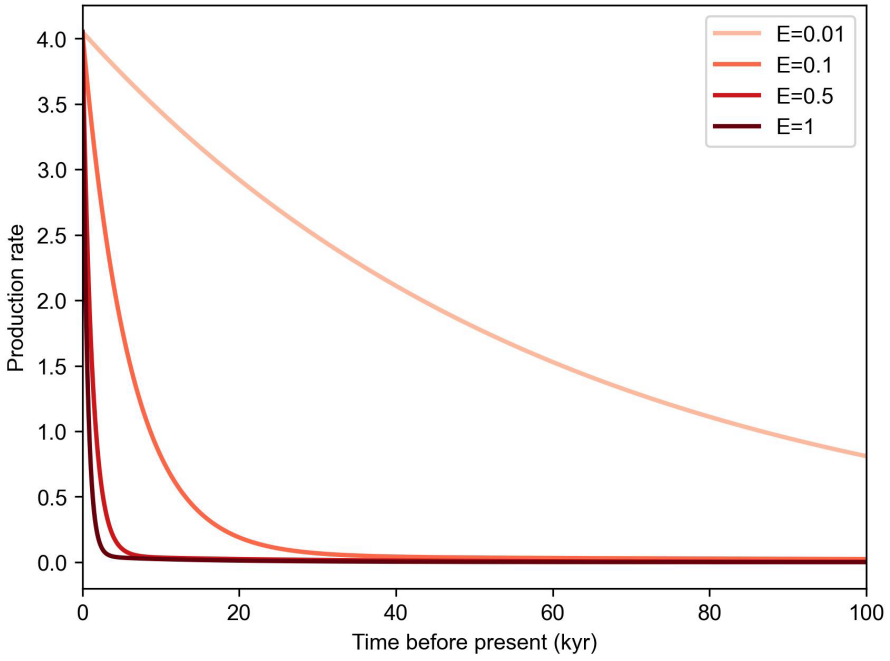


Fig. 10. Temporal evolution of cosmogenic nuclide production rates before present for a range of erosion rates (mm/yr). Production rates are expressed in atoms/(g*yr).

5.3 Applicability to natural landscapes and cosmogenic-nuclide systems

The practical application of $E_{cos\text{-}Qm}$ and $k_{s\text{-}Qeff}$ to natural landscapes is primarily limited by uncertainties in paleo-precipitation reconstructions, the coupled variability of uplift and precipitation histories, and the nuclide-dependent timescale of cosmogenic erosion-rate signals.

Reconstructing paleo-precipitation remains one of the major challenges in paleoclimatology, introducing uncertainty into the estimation of $E_{cos\text{-}Qm}$ and $k_{s\text{-}Qeff}$. Proxy records, such as stalagmites or loess deposits, can reliably indicate relative changes between wetter and drier periods at specific sites, but their spatial resolution is limited due to the sparse distribution of available records. Moreover, translating these proxies into quantitative precipitation estimates is inherently difficult. Paleoclimate models, by contrast, offer broad spatial coverage and high spatial resolution. In this study, we use the CHELSA-TraCE21k climate model (Karger et al., 2021), which provides precipitation at ~1 km spatial resolution from 21 ka to the present. This model is based on the TraCE-21k (Transient Climate Evolution of the last 21,000 years) simulation (Liu et al., 2009; He, 2011), which includes atmosphere, ocean, land, sea ice, and vegetation components, and captures large-scale climate evolution since the Last Glacial Maximum, though at coarse spatial resolution. By applying downscaling approaches that incorporate present-day climatology, glacier extent, topography, and sea-level changes, CHELSA-TraCE21k (Karger et al., 2021) reconstructs paleo-orography and accounts for orographic effects, providing spatially continuous and temporally

https://doi.org/10.5194/egusphere-2026-4732
Preprint. Discussion started: 2 November 2026
© Author(s) 2026. CC BY 4.0 License.

evolving precipitation fields at high resolution. This makes it particularly suitable for investigating climatic variability and its geomorphic implications. The transient nature of the CHELSA-TraCE21k dataset allows us to explore how climatic cycles may influence erosion rates and channel steepness, which are sensitive to temporal variability in forcing. It is important to note that this dataset represents a model-based reconstruction rather than direct observations. Accordingly, several sources of uncertainty should be acknowledged. The dataset relies on bias correction methods that assume temporally constant model biases, and glacier dynamics are largely controlled by temperature, which may oversimplify processes in glaciated regions. In addition, precipitation patterns in complex mountainous terrain remain difficult to resolve, and paleo-topography introduces further uncertainty, particularly in regions such as the TRR, where mountain morphology exerts a strong influence on precipitation (Xiang et al., 2024). To extend the precipitation history beyond 21 ka, we apply a proxy-informed fitting approach to reconstruct variability back to 100 ka. While this extrapolation introduces additional uncertainty, it preserves the dominant cyclic signals that are central to our analysis. Overall, despite these limitations, the CHELSA-TraCE21k dataset provides a reasonable framework for capturing the first-order spatial and temporal patterns of precipitation, which is sufficient for evaluating the role of climatic cycles in shaping erosion and channel steepness.

A second challenge arises from the fact that natural catchments rarely differ only in precipitation history. Catchments typically exhibit variations in both uplift and precipitation, making it necessary to assess their relative effects. As shown in Fig. 3, although the absolute amplitudes of E_{cos} increase with higher uplift rates (Fig. 3a), their normalized amplitudes, defined as the absolute amplitude of E_{cos} divided by $E_{cos\text{-}Qm}$, remain nearly constant across different uplift scenarios (Fig. 3b). Similarly, the absolute amplitudes of $k_{s\text{-}Q}$ increase with uplift (Fig. 3c), whereas the normalized $k_{s\text{-}Q}$ amplitudes, calculated as the absolute amplitude of $k_{s\text{-}Q}$ divided by $k_{s\text{-}Qeff}$, show consistent patterns regardless of uplift rate (Fig. 3d). In the TRR, E_{cos} values range from 0 to ~0.6 mm/yr, suggesting substantial spatial variability in uplift rate. Under these conditions, relative differences in erosion rates and channel steepness provide a more robust basis for isolating the influence of precipitation.

A further consideration is the choice of cosmogenic nuclide. Although the calculations presented in this study are based on ^{10}Be parameters, the $E_{cos\text{-}Qm}$ framework can, in principle, be extended to other cosmogenic nuclides by using the appropriate production rates, attenuation lengths, and decay constants. However, the response to Milankovitch-scale precipitation variability is expected to depend on both nuclide properties and erosion rate, because different nuclides have different half-lives and then different effective integration timescales. Short-lived nuclides, such as in situ ^{14}C, have shorter half-lives than ^{10}Be and may therefore be more sensitive to recent changes in erosion rate (Skov et al., 2019). As a result, in situ ^{14}C -derived erosion rates may more closely reflect recent or near-instantaneous erosion conditions. This nuclide-dependent sensitivity implies that the response to precipitation cycles of different periods, as shown in Fig. 4 for ^{10}Be, may differ when other cosmogenic nuclides are used.

5.4 River behavior assumptions

This study is based on simplifying assumptions about river dynamics. First, our modelling framework focuses on channel incision and does not explicitly represent hillslope processes. This simplification may be important because hillslope erosion

https://doi.org/10.5194/egusphere-2026-4732
Preprint. Discussion started: 2 November 2026
© Author(s) 2026. CC BY 4.0 License.

rates and sediment-production mechanisms can vary with precipitation and with the rate of channel incision at the hillslope boundary (Owen et al., 2011). If hillslope erosion responds differently or more slowly than channel incision under temporally varying precipitation, catchment-averaged cosmogenic erosion rates may not directly track the channel-incision response predicted by the model. Our results are therefore most directly applicable where channel incision and hillslope sediment production remain closely coupled.

Second, our model assumes detachment-limited incision and does not explicitly represent sediment transport or erosion thresholds. In systems with substantial sediment transport and storage, adjustments in channel gradient and sediment flux may modify the transmission of precipitation-driven signals (Simpson and Castelltort, 2012), with the magnitude of the sediment-flux response also varying with the forcing period (Godard et al., 2013). Our results are therefore most applicable to bedrock rivers in which incision is primarily limited by detachment from the channel bed.

6 Conclusions

This study demonstrates that temporal cyclic variations in precipitation, particularly those associated with Milankovitch-scale climate cycles, can significantly influence the interpretation of erosion rate-channel steepness relationships. Using a one-dimensional stream power-based river profile model that incorporates cyclic precipitation, we show that Milankovitch-scale cycles represent an effective timescale for precipitation to modulate instantaneous erosion rates (E_{in}), cosmogenic erosion rates (E_{cos}), and precipitation-modified channel steepness ($k_{s\text{-}Q}$). When the precipitation period is long, E_{cos} closely tracks E_{in} with minimal lag relative to $k_{s\text{-}Q}$. Conversely, when the period is short, E_{cos} effectively reflects long-term erosion rates or uplift. Among the parameters examined, the ratio of precipitation amplitude to mean precipitation (P_a / P_m) emerges as the dominant control on the deviation of E_{cos} and $k_{s\text{-}Q}$ from long-term erosion rates and the corresponding channel steepness value. In regions with high P_a / P_m values, these deviations become substantial. In extreme cases, phase mismatches can even reverse the expected relationship between these metrics.

To address these limitations, we propose combining two climate-integrated metrics: the cosmogenic-constrained cycle-mean erosion rate ($E_{cos\text{-}Qm}$), introduced in this study, and the effective precipitation-modified steepness index ($k_{s\text{-}Qeff}$), developed in earlier work. $E_{cos\text{-}Qm}$ can be derived from measured ^{10}Be concentrations in combination with a known precipitation history, while $k_{s\text{-}Qeff}$ accounts for precipitation averaged over a climatic cycle. Together, these metrics offer more robust indicators of long-term uplift, remaining stable under both sinusoidal and proxy-based climate forcing.

Application to the Three Rivers region confirms their utility, albeit with a small effect. Catchments with higher P_a / P_m values show larger discrepancies between E_{cos} and $E_{cos\text{-}Qm}$, and between $k_{sn\text{-}Q}$ and $k_{sn\text{-}Qeff}$, reinforcing the importance of accounting for temporal precipitation variability in erosion rate-channel steepness analyses.

Overall, our findings highlight the potential for misinterpretation when climatic cyclicity is ignored, particularly in regions with high P_a / P_m values. Climate-informed metrics such as $E_{cos\text{-}Qm}$ and $k_{s\text{-}Qeff}$ provide a more accurate framework for linking surface processes to tectonic forcing over Milankovitch timescales.

https://doi.org/10.5194/egusphere-2026-4732
Preprint. Discussion started: 2 November 2026
© Author(s) 2026. CC BY 4.0 License.

Code and data availability

Python scripts and data used in this study are available online on Zenodo (https://doi.org/10.5281/zenodo.21822492).

Author contributions

Xianjun Fang: Writing-review & editing, Writing-original draft, Conceptualization, Methodology, Formal analysis, Visualization.

Sean D. Willett: Writing-review & editing, Writing-original draft, Conceptualization, Funding acquisition, Supervision, Methodology.

Declaration of competing interest

The authors declare that they do not have any financial interests or personal relationships that could have affected the objectivity of this work.

Acknowledgements

This study was funded by ETH Zurich (Biodiversity, Earth, Climate Coupling in Yunnan, BECCY project). We gratefully acknowledge Eric Deal and Lindsay Schoenbohm for feedback.

References

Adams, B.A., Whipple, K.X., Forte, A.M., Heimsath, A.M., Hodges, K.V., 2020. Climate controls on erosion in tectonically active landscapes. Sci. Adv. 6, eaaz3166. https://doi.org/10.1126/sciadv.aaz3166

Ao, H., Dekkers, M.J., Xiao, G., Yang, X., Qin, L., Liu, X., Qiang, X., Chang, H., Zhao, H., 2012. Different orbital rhythms in the Asian summer monsoon records from North and South China during the Pleistocene. Glob. Planet. Change 80–81, 51–60. https://doi.org/10.1016/j.gloplacha.2011.09.012

Borchers, B., Marrero, S., Balco, G., Caffee, M., Goehring, B., Lifton, N., Nishiizumi, K., Phillips, F., Schaefer, J., Stone, J., 2016. Geological calibration of spallation production rates in the CRONUS-Earth project. Quat. Geochronol. 31, 188–198. https://doi.org/10.1016/j.quageo.2015.01.009

Braucher, R., Merchel, S., Borgomano, J., Bourlès, D.L., 2011. Production of cosmogenic radionuclides at great depth: A multi element approach. Earth Planet. Sci. Lett. 309, 1–9. https://doi.org/10.1016/j.epsl.2011.06.036

https://doi.org/10.5194/egusphere-2026-4732
Preprint. Discussion started: 2 November 2026
© Author(s) 2026. CC BY 4.0 License.

Brown, E.T., Stallard, R.F., Larsen, M.C., Raisbeck, G.M., Yiou, F., 1995. Denudation rates determined from the accumulation of in situ-produced 10Be in the luquillo experimental forest, Puerto Rico. Earth Planet. Sci. Lett. 129, 193–202. https://doi.org/10.1016/0012-821X(94)00249-X

Cai, Y., Fung, I.Y., Edwards, R.L., An, Z., Cheng, H., Lee, J.-E., Tan, L., Shen, C.-C., Wang, X., Day, J.A., Zhou, W., Kelly, M.J., Chiang, J.C.H., 2015. Variability of stalagmite-inferred Indian monsoon precipitation over the past 252,000 y. Proc. Natl. Acad. Sci. 112, 2954–2959. https://doi.org/10.1073/pnas.1424035112

Cheng, H., Edwards, R.L., Sinha, A., Spötl, C., Yi, L., Chen, S., Kelly, M., Kathayat, G., Wang, X., Li, X., Kong, X., Wang, Y., Ning, Y., Zhang, H., 2016. The Asian monsoon over the past 640,000 years and ice age terminations. Nature 534, 640–646. https://doi.org/10.1038/nature18591

Chmeleff, J., Von Blanckenburg, F., Kossert, K., Jakob, D., 2010. Determination of the 10Be half-life by multicollector ICP-MS and liquid scintillation counting. Nucl. Instrum. Methods Phys. Res. Sect. B Beam Interact. Mater. At. 268, 192–199. https://doi.org/10.1016/j.nimb.2009.09.012

DiBiase, R.A., Whipple, K.X., Heimsath, A.M., Ouimet, W.B., 2010. Landscape form and millennial erosion rates in the San Gabriel Mountains, CA. Earth Planet. Sci. Lett. 289, 134–144. https://doi.org/10.1016/j.epsl.2009.10.036

Dykoski, C., Edwards, R., Cheng, H., Yuan, D., Cai, Y., Zhang, M., Lin, Y., Qing, J., An, Z., Revenaugh, J., 2005. A high-resolution, absolute-dated Holocene and deglacial Asian monsoon record from Dongge Cave, China. Earth Planet. Sci. Lett. 233, 71–86. https://doi.org/10.1016/j.epsl.2005.01.036

Fang, X., Willett, S.D., Yang, R., Scherler, D., Haghipour, N., Christl, M., 2026. Local and regional tectonic controls on spatial patterns of erosion rate and topography in the Three Rivers Region, southeastern Tibetan Plateau. Earth Planet. Sci. Lett. 688, 120099. https://doi.org/10.1016/j.epsl.2026.120099

Ferrier, K.L., Huppert, K.L., Perron, J.T., 2013. Climatic control of bedrock river incision. Nature 496, 206–209. https://doi.org/10.1038/nature11982

Finlayson, D.P., Montgomery, D.R., 2003. Modeling large-scale fluvial erosion in geographic information systems. Geomorphology 53, 147–164. https://doi.org/10.1016/S0169-555X(02)00351-3

Godard, V., Tucker, G.E., Burch Fisher, G., Burbank, D.W., Bookhagen, B., 2013. Frequency-dependent landscape response to climatic forcing. Geophys. Res. Lett. 40, 859–863. https://doi.org/10.1002/grl.50253

Goren, L., 2016. A theoretical model for fluvial channel response time during time-dependent climatic and tectonic forcing and its inverse applications. Geophys. Res. Lett. 43. https://doi.org/10.1002/2016GL070451

Hack, J.T., 1957. Studies of Longitudinal Stream Profiles in Virginia and Maryland. US Government Printing Office.

Han, H.K., Gomez, N., Pollard, D., DeConto, R., 2021. Modeling Northern Hemispheric Ice Sheet Dynamics, Sea Level Change, and Solid Earth Deformation Through the Last Glacial Cycle. J. Geophys. Res. Earth Surf. 126, e2020JF006040. https://doi.org/10.1029/2020JF006040

Harel, M.-A., Mudd, S.M., Attal, M., 2016. Global analysis of the stream power law parameters based on worldwide 10Be denudation rates. Geomorphology 268, 184–196. https://doi.org/10.1016/j.geomorph.2016.05.035

© Author(s) 2026. CC BY 4.0 License.

Henck, A.C., Huntington, K.W., Stone, J.O., Montgomery, D.R., Hallet, B., 2011. Spatial controls on erosion in the Three Rivers Region, southeastern Tibet and southwestern China. Earth Planet. Sci. Lett. 303, 71–83. https://doi.org/10.1016/j.epsl.2010.12.038

Howard, A.D., 1994. A detachment-limited model of drainage catchment evolution. Water Resour. Res. 30, 2261–2285. https://doi.org/10.1029/94WR00757

Howard, A.D., Kerby, G., 1983. Channel changes in badlands. Geol. Soc. Am. Bull. 94, 739. https://doi.org/10.1130/0016-7606(1983)94<739:CCIB>2.0.CO;2

Hu, G., Yi, C.-L., Zhang, J.-F., Liu, J.-H., Jiang, T., Qin, X., 2014. Optically stimulated luminescence dating of a moraine and a terrace in Laohugou valley, western Qilian Shan, northeastern Tibet. Quat. Int. 321, 37–49. https://doi.org/10.1016/j.quaint.2013.12.019

Kageyama, M., Harrison, S.P., Kapsch, M.-L., Lofverstrom, M., Lora, J.M., Mikolajewicz, U., Sherriff-Tadano, S., Vadsaria, T., Abe-Ouchi, A., Bouttes, N., Chandan, D., Gregoire, L.J., Ivanovic, R.F., Izumi, K., LeGrande, A.N., Lhardy, F., Lohmann, G., Morozova, P.A., Ohgaito, R., Paul, A., Peltier, W.R., Poulsen, C.J., Quiquet, A., Roche, D.M., Shi, X., Tierney, J.E., Valdes, P.J., Volodin, E., Zhu, J., 2021. The PMIP4 Last Glacial Maximum experiments: preliminary results and comparison with the PMIP3 simulations. Clim. Past 17, 1065–1089. https://doi.org/10.5194/cp-17-1065-2021

Karger, D.N., Nobis, M.P., Normand, S., Graham, C.H., Zimmermann, N.E., 2021. CHELSA-TraCE21k v1.0. Downscaled transient temperature and precipitation data since the last glacial maximum. https://doi.org/10.5194/cp-2021-30

Kotlia, B.S., Sanwal, J., Phartiyal, B., Joshi, L.M., Trivedi, A., Sharma, C., 2010. Late Quaternary climatic changes in the eastern Kumaun Himalaya, India, as deduced from multi-proxy studies. Quat. Int. 213, 44–55. https://doi.org/10.1016/j.quaint.2009.09.002

Lague, D., 2014. The stream power river incision model: evidence, theory and beyond. Earth Surf. Process. Landf. 39, 38–61. https://doi.org/10.1002/esp.3462

Laskar, J., Robutel, P., Joutel, F., Gastineau, M., Correia, A.C.M., Levrard, B., 2004. A long-term numerical solution for the insolation quantities of the Earth. Astron. Astrophys. 428, 261–285. https://doi.org/10.1051/0004-6361:20041335

Leonard, J.S., Whipple, K.X., 2021. Influence of Spatial Rainfall Gradients on River Longitudinal Profiles and the Topographic Expression of Spatially and Temporally Variable Climates in Mountain Landscapes. J. Geophys. Res. Earth Surf. 126, e2021JF006183. https://doi.org/10.1029/2021JF006183

Leonard, J.S., Whipple, K.X., Heimsath, A.M., 2024. Controls on topography and erosion of the north-central Andes. Geology 52, 153–158. https://doi.org/10.1130/G51618.1

Li, J., Ehlers, T.A., Werner, M., Mutz, S.G., Steger, C., Paeth, H., 2017. Late quaternary climate, precipitation δ18O, and Indian monsoon variations over the Tibetan Plateau. Earth Planet. Sci. Lett. 457, 412–422. https://doi.org/10.1016/j.epsl.2016.09.031

Lisiecki, L.E., Raymo, M.E., 2005. A Pliocene-Pleistocene stack of 57 globally distributed benthic δ 18 O records. Paleoceanography 20, 2004PA001071. https://doi.org/10.1029/2004PA001071

https://doi.org/10.5194/egusphere-2026-4732
Preprint. Discussion started: 2 November 2026
© Author(s) 2026. CC BY 4.0 License.

Marder, E., Gallen, S.F., 2023. Climate control on the relationship between erosion rate and fluvial topography. Geology 51, 424–427. https://doi.org/10.1130/G50832.1

Mudd, S.M., 2017. Detection of transience in eroding landscapes. Earth Surf. Process. Landf. 42, 24–41. https://doi.org/10.1002/esp.3923

Mutz, S.G., Ehlers, T.A., Werner, M., Lohmann, G., Stepanek, C., Li, J., 2018. Estimates of late Cenozoic climate change relevant to Earth surface processes in tectonically active orogens. Earth Surf. Dyn. 6, 271–301. https://doi.org/10.5194/esurf-6-271-2018

Ouimet, W.B., Whipple, K.X., Granger, D.E., 2009. Beyond threshold hillslopes: Channel adjustment to base-level fall in tectonically active mountain ranges. Geology 37, 579–582. https://doi.org/10.1130/G30013A.1

Owen, J.J., Amundson, R., Dietrich, W.E., Nishiizumi, K., Sutter, B., Chong, G., 2011. The sensitivity of hillslope bedrock erosion to precipitation. Earth Surf. Process. Landf. 36, 117–135. https://doi.org/10.1002/esp.2083

Perron, J.T., Royden, L., 2013. An integral approach to bedrock river profile analysis. Earth Surf. Process. Landf. 38, 570–576. https://doi.org/10.1002/esp.3302

Roe, G.H., Montgomery, D.R., Hallet, B., 2002. Effects of orographic precipitation variations on the concavity of steady-state river profiles. Geology 30, 143. https://doi.org/10.1130/0091-7613(2002)030%3C0143:EOOPVO%3E2.0.CO;2

Simpson, G., Castelltort, S., 2012. Model shows that rivers transmit high-frequency climate cycles to the sedimentary record. Geology 40, 1131–1134. https://doi.org/10.1130/G33451.1

Skov, D.S., Egholm, D.L., Jansen, J.D., Sandiford, M., Knudsen, M.F., 2019. Detecting landscape transience with in situ cosmogenic 14C and 10Be. Quat. Geochronol. 54, 101008. https://doi.org/10.1016/j.quageo.2019.101008

Tucker, G.E., Slingerland, R.L., 1994. Erosional dynamics, flexural isostasy, and long-lived escarpments: A numerical modeling study. J. Geophys. Res. Solid Earth 99, 12229–12243. https://doi.org/10.1029/94JB00320

Wang, R.L., Scarpitta, S.C., Zhang, S.C., Zheng, M.P., 2002. Later Pleistocene/Holocene climate conditions of Qinghai–Xizhang Plateau (Tibet) based on carbon and oxygen stable isotopes of Zabuye Lake sediments. Earth Planet. Sci. Lett. 203, 461–477. https://doi.org/10.1016/s0012-821x(02)00829-4

Wang, Y.J., Cheng, H., Edwards, R.L., An, Z.S., Wu, J.Y., Shen, C.-C., Dorale, J.A., 2001. A High-Resolution Absolute-Dated Late Pleistocene Monsoon Record from Hulu Cave, China. Science 294, 2345–2348. https://doi.org/10.1126/science.1064618

Whipple, K., Adams, B., Forte, A., Hodges, K., 2023. Eroding the Himalaya: Topographic and Climatic Control of Erosion Rates and Implications for Tectonics. J. Geol. 131, 265–288. https://doi.org/10.1086/731260

Whipple, K.X., Tucker, G.E., 1999. Dynamics of the stream-power river incision model: Implications for height limits of mountain ranges, landscape response timescales, and research needs. J. Geophys. Res. Solid Earth 104, 17661–17674. https://doi.org/10.1029/1999JB900120

Wolpert, J.A., Schoenbohm, L.M., 2025. Channel Steepness Biases and Nonsteady Erosion in Landscapes Evolving Under Cyclical Climate. Geophys. Res. Lett. 52, e2024GL112229. https://doi.org/10.1029/2024GL112229

https://doi.org/10.5194/egusphere-2026-4732
Preprint. Discussion started: 2 November 2026
© Author(s) 2026. CC BY 4.0 License.



Xiang, R., Steger, C.R., Li, S., Pellissier, L., Sørland, S.L., Willett, S.D., Schär, C., 2024. Assessing the Regional Climate Response to Different Hengduan Mountains Geometries With a High-Resolution Regional Climate Model. J. Geophys. Res. Atmospheres 129, e2023JD040208. https://doi.org/10.1029/2023JD040208

Yang, R., Willett, S.D., Goren, L., 2015. In situ low-relief landscape formation as a result of river network disruption. Nature 520, 526–529. https://doi.org/10.1038/nature14354